NASA
Technical
Paper
3156

November 1991

Transonic and Supersonic Euler Computations of Vortex-Dominated Flow Fields About a Generic Fighter

Aga M. Goodsell
and John E. Melton

NASA

NASA Technical Paper 3156

1991

Transonic and Supersonic Euler Computations of Vortex-Dominated Flow Fields About a Generic Fighter

Aga M. Goodsell
and John E. Melton
Ames Research Center
Moffett Field, California

NASA
National Aeronautics and Space Administration
Office of Management
Scientific and Technical Information Program

SUMMARY

Flow fields about a generic fighter model have been computed using FLO57, a three-dimensional, finite-volume Euler code. Computed pressure coefficients, forces, and moments at several Mach numbers—0.6, 0.8, 1.2, 1.4, and 1.6—are compared with wind tunnel data over a wide range of angles of attack in order to determine the applicability of the code for the analysis of fighter configurations. Two configurations were studied, a wing/body and a wing/body/chine. FLO57 predicted pressure distributions, forces, and moments well at low angles of attack, at which the flow was fully attached. The FLO57 predictions were also accurate for some test conditions once the leading-edge vortex became well established. At the subsonic speeds, FLO57 predicted vortex breakdown earlier than that seen in the experimental results. Placing the chine on the forebody delayed the onset of bursting and improved the correlation between numerical and experimental data at the subsonic conditions.

INTRODUCTION

It is common for modern fighter aircraft to maneuver at high angles of attack and to achieve maximum lift at angles as large as 25° to 30°. Vortices resulting from flow separation at the wing leading edges and from the fuselage forebody dominate the flow field at these angles. Since these vortical flows can greatly increase the controllable angle-of-attack range, they are currently the topic of much study, both experimentally and computationally.

A large amount of work has been done at subsonic and supersonic speeds to provide a good understanding of the mechanisms involved in the formation and effects of the leading-edge vortices on delta wings. In a subsonic free-stream condition, the flow undergoes a strong expansion at the leading edge from the windward to the leeward side. For sharp leading edges, the boundary layer cannot overcome the strong adverse pressure gradient that results from the recompression on the leeward edge just inboard of the expansion, and the flow separates at the leading edge producing a free-shear layer of distributed vorticity. The separation point is fixed at the leading edge for all angles of attack above that for initial separation and is independent of boundary-layer condition or leading-edge geometry (ref. 1). These leeward vortices, which occur in counterrotating pairs as the flow is shed from opposite leading edges, are the dominant features of the flow. The vortices induce very low pressure levels on the wing surface directly below the vortex core. The resultant normal force is then much larger than that which would occur if the flow were to remain attached and the vortices were not present (ref. 1). Secondary and tertiary vortices may form on the leeward surface of the wing if the flow in the boundary layer cannot overcome the adverse pressure gradient that exists under the primary vortex core. At supersonic speeds, experiments have shown that on highly swept wings with subsonic leading edges, the upper surface flow is similar to that at low speeds. As the Mach number increases or the sweep angle decreases, the vortices become flatter and eventually disappear, giving way to attached flow at the leading edge (ref. 2). Further descriptions of the underlying physical phenomena for these vortical flows are contained in the works of Stanbrook and Squire (ref. 3) and Miller and Wood (ref. 4). The physical complexity of the flow field at transonic speeds is not well understood because of the existence of shock waves, vortex–shock interactions, vortex breakdown, and shock–boundary-layer interaction.

The objective of this paper is to evaluate the solutions of transonic and low supersonic flow fields about a generic fighter with delta wings obtained from an Euler code in order to determine their validity over a wide range of angles of attack. The Navier–Stokes equations correctly model the relevant flow physics and provide a uniformly valid description of vortical flow about arbitrary geometries throughout the range of flight speeds and Reynolds numbers. However, numerical simulations of these equations require more memory and CPU time. The Euler equations provide the correct Rankine–Hugoniot shock jump conditions and allow for the transport of vorticity, but cannot model the viscous effects present in the flow field.

EXPERIMENTAL WORK

In an effort to increase the understanding of vortex flows at transonic speeds, Erickson and Rogers (ref. 2) and Erickson and Schreiner (ref. 5) conducted a series of experimental investigations into the behavior of the generic fighter model at transonic conditions.

The model had a 55° swept cropped delta wing of aspect ratio 1.8 and taper ratio 0.2. The airfoils used in the wing were modified NACA 65A005 sections with sharp leading edges. A chine with wedge cross section was added to the forebody 0.5 in. above the wing. See figure 1 for the planform view, side view, and two cross-sectional views of the model. The model was equipped with a total of 80 upper-surface static pressure taps located at 30%, 40%, 50%, 62.5%, and 75% of the distance along the wing centerline chord as depicted in figure 1. The wing was mounted on a generic fuselage that accommodated a four-module Scanivalve and a six-component balance.

The model was tested in the David Taylor Naval Ship Research and Development Center's 7- by 10-ft transonic tunnel at Mach numbers between 0.40 and 0.95 and at angles of attack between 0° and 22°. The effects of Mach number, angle of attack, and the leading-edge flap deflection on the wing upper-surface static pressure distributions were studied (ref. 2). The model was also tested in the NASA Ames Research Center's 6- by 6-ft wind tunnel at Mach numbers between 0.40 and 1.8, and at angles of attack between 0° and 24°. The emphasis in the Ames test was to determine the changes in the flow field over the wing made by placing a chine at various locations on the forebody (ref. 5).

COMPUTATIONAL WORK

Computational fluid dynamics (CFD) is becoming increasingly important in the analysis and understanding of flows about complex configurations. Wind tunnel data is often limited by instrumentation constraints, flow quality, wall and support interferences, and aeroelastic effects. In contrast, CFD codes provide detailed information about the entire flow field, thus they are helpful in understanding off-body flow-field characteristics. The validation of CFD codes for a wide range of flight conditions is essential if they are to become useful tools in aerodynamic design and analysis. With the advent of supercomputers such as the Cray–2 and the Cray Y–MP, it is now possible to compute Euler and Navier–Stokes solutions for complex geometries using denser grids, thus improving upon the accuracy of the solutions obtained in the past. The numerical solutions of the Euler and Navier–Stokes equations are not yet at the production level at which they can be easily applied to any configuration and flight condition. The generation of a suitable grid about a complex configuration remains one of the most challenging problems in the field of CFD.

Euler Solution Procedure

The Euler equations govern the adiabatic flow of an inviscid, ideal gas. For a three-dimensional, unsteady flow the Euler equations in conservation form are

$$\frac{\partial}{\partial t}\begin{pmatrix}\rho\\ \rho u\\ \rho v\\ \rho w\\ \rho E\end{pmatrix}+\frac{\partial}{\partial x}\begin{pmatrix}\rho u\\ \rho u^2+p\\ \rho uv\\ \rho uw\\ \rho uh_0\end{pmatrix}+\frac{\partial}{\partial y}\begin{pmatrix}\rho v\\ \rho uv\\ \rho v^2+p\\ \rho vw\\ \rho vh_0\end{pmatrix}+\frac{\partial}{\partial z}\begin{pmatrix}\rho w\\ \rho uw\\ \rho vw\\ \rho w^2+p\\ \rho wh_0\end{pmatrix}=0 \tag{1}$$

where ρ is the density, p is the pressure, u, v, w are the Cartesian velocity components, E is the total energy per unit mass, and h_0 is the total enthalpy per unit mass. The equation of state

$$\frac{p}{\rho}=(\gamma-1)\left[E-\frac{u^2+v^2+w^2}{2}\right] \tag{2}$$

and the supplementary relation

$$h_0=E+\frac{p}{\rho} \tag{3}$$

close the set of equations. The tangential flow boundary condition is enforced on the solid body whereas the Kutta condition at the sharp leading and trailing edges is held implicitly in the numerical integration (ref. 6). The application of Euler methods to the prediction of vortical flow about delta wings and slender bodies at angle of attack remains the source of considerable controversy. How separation occurs in the numerical simulation of an inviscid flow, and the degree of realism that the inviscid model provides in describing the actual flow physics, have not yet been thoroughly established. Following Newsome (ref. 1), Crocco's theorem is applied to show that theoretically valid solutions to the Euler equations with flow separation do exist. However, the solutions do not necessarily provide an accurate description of the separation that occurs in

the actual viscous flow (ref. 7). Numerical solutions of separated flows can be explained by the addition of dissipation in the computational algorithm required for stability. Several studies have been performed to examine the effect of dissipation on the solutions of flows about delta wings. Powell, et al. (ref. 8), have argued that a Kutta condition exists at a sharp leading edge that fixes the point of separation at the leading edge independent of the amount of dissipation added. The only requirement is that the computational model have a diffusive effect at the leading edge that mimics physical viscous diffusion. Because of truncation error and added artificial viscosity, the discretized Euler equations are diffusive near the leading edge.

The numerical algorithm FLO57 was originally written by Jameson (ref. 9) and was modified by Melton to accommodate an O–H grid topology. The method is a finite-volume multistage technique which is second-order accurate on a smooth grid. Since the numerical algorithm is not inherently dissipative, artificial viscosity must be added to the discretized equations to provide stability. The added dissipation includes second- and fourth-difference terms. The fourth-difference term is third order and provides dissipation in smooth regions. The second-difference term is proportional to the second difference in pressure, and is first order. This term limits shock oscillations, thereby allowing shock capturing, and is significant in regions of rapid expansion.

The grid generated about the generic fighter has an O–H topology which allows good leading-edge resolution compared to other topologies. The grid was generated using an elliptic solver which was written by Melton. This code solves the Laplace equation in two dimensions in order to smoothly wrap a grid around the body at specific longitudinal locations. This grid is then algebraically redistributed in the direction normal to the wing surface to provide a user-specified clustering near the wing surface and also to provide a smooth transition between grid planes in the streamwise direction.

The grid used in all of the computations has 426,790 grid points: 134 points in the streamwise direction with 74 points on the body, 49 points from the wing surface to the outer boundary, and 65 points circumferentially around the body. The grid extends 6.5 centerline chord lengths upstream and downstream of the body and 7 semispan lengths radially to the outer boundary. The chine was modeled as a flat plate. The surface grid for the wing/body model is shown in figure 2.

RESULTS/DISCUSSION

FLO57 solutions were obtained at Mach numbers of 0.6, 0.8, and 1.2 for the wing/body configuration and 0.6, 0.8, 1.2, 1.4, and 1.6 for the wing/body/chine configuration. A minimum of 1200 iterations at the low angles of attack and 3000 to 3500 iterations at the higher angles were necessary to ensure that the residuals decreased at least three orders of magnitude. The lift, drag, and moment histories show convergence after about 1000 iterations while the residuals are still decreasing. All solutions were obtained on either the Cray–2 or the Cray Y–MP at NASA Ames Research Center. The memory requirement was approximately 12 MW, and the CPU time required for 1000 iterations was approximately 10,300 sec on the Cray–2 and approximately 4800 sec on the Cray Y–MP. Thus, each solution took 4 to 10 hr to obtain on the Cray–2 and 2 to 4 hr on the Cray Y–MP. Computed pressure coefficients at the 30%, 40%, 50%, 62.5%, and 75% chord stations along with lift, drag, and pitching moment for each Mach–alpha combination were compared to the experimental results. A discussion of the results for each combination of Mach number and configuration will be presented in the following sections.

Mach 0.6 Wing/Body

At $M_\infty = 0.6$, the FLO57 pressure distributions compare well with experimental results at $\alpha = 4°$, where the flow is attached and there is no leading-edge vortex (figs. 3(a)–3(d)). The shape of the pressure distribution is accurately modeled.

The experimental results show that a vortex has begun to form close to the leading edge at $\alpha = 8°$ (figs. 4(a)–4(d)). The numerical results do not correlate as well with experimental results as they do at the lower angle of attack. The Euler results show the formation of a weaker vortex that lies inboard of the experimental vortex. Since the vortex is just starting to form, the Euler solution may be sensitive to the grid density and the numerical definition of the leading-edge geometry.

The vortex strengthens and moves inboard at $\alpha = 12°$, as shown in figures 5(a)–5(d). At 40% chord, the Euler results capture the strength and position of the primary vortex accurately. Farther aft on the wing,

the secondary separation and other viscous effects can be seen in the experimental pressure distributions and in the oil flow (see photo, fig. 6). The secondary separation moves the primary vortex inboard and creates a low-pressure region extending outboard from the core of the primary vortex. These flow characteristics cannot be modeled with the Euler equations. FLO57 predicts a stronger primary vortex that lies outboard of the experimental vortex at 50% and 62.5% chord. At 75% chord the Euler results show a flattening of the vortex core, which suggests that the vortex is breaking down at this point. Further evidence of vortex breakdown is given by numerical simulations of particle paths which show recirculation within the vortex core.

Vortex bursting is apparent in both computational and experimental pressure distributions at $\alpha = 16°$ (figs. 7(a)–7(d)) and 20° (figs. 8(a)–8(d)). In addition, oil flow photos show an abrupt expansion of the vortex after approximately 50% chord, which is an indication of vortex breakdown (see figs. 9 and 10). Aft of the breakdown position, the vortex structure is no longer maintained and the pressure distributions become unsteady. Numerical vortex bursting is confirmed by the unstable and oscillatory moment histories that were observed at the higher angles of attack (fig. 11). At both angles FLO57 predicts the burst location ahead of that seen in the wind tunnel data. At stations where breakdown has occurred both in experiment and in computations, the agreement between Euler and experimental results improves. The existence of a cross-flow shock in the region near the wing apex is also seen in the experimental pressure distributions and oil flow photos, but is not apparent in the FLO57 results. The reason a cross-flow shock may not appear in the Euler computations is that at the stations between the apex and 50% chord the grid lacks the resolution required to capture the shock.

Comparisons between the computational and experimental force coefficients show that FLO57 predicts the lift and drag well until about $\alpha = 16°$ at which the vortex is burst over much of the wing (figs. 12(a) and 12(b)). Moment predictions do not agree well with experiment above $\alpha = 8°$ (fig. 12(c)). The balance moment center was located at 69.4% of the centerline chordlength. However, the angle at which the slope of the moment curve changes as predicted by FLO57 is in good agreement with wind tunnel data.

Mach 0.6 Wing/Body/Chine

The overall agreement between computational and experimental results improved with the addition of the chine. Without the chine, the flow over the forebody is strongly affected by viscous separations. These effects cannot be modeled in an Euler simulation. The dominant vortex from the chine is captured by the Euler code, allowing FLO57 to provide a more representative model of the forebody flow field as it approaches the apex of the main wing.

The shape of the pressure distribution is well modeled by the Euler code at $\alpha = 4°$ (figs. 13(a)–13(d)). At $\alpha = 8°$, the Euler code has difficulty modeling the start of the vortex as previously described, and the correlation is not as good (see figs. 14(a)–14(d)).

The pressure distributions at $\alpha = 12°$ are shown in figures 15(a)–15(d). At 40% and 50% chord, the Euler results accurately predict the location and strength of the vortex. At 62.5% and 75% chord, the computational results show that the vortex is slightly outboard and stronger than in the experiment. This is due to the stronger influence of the secondary separation at the stations farther downstream.

Both Euler and experimental results at $\alpha = 16°$ (figs. 16(a)–16(d)) and $\alpha = 20°$ (figs. 17(a)–17(d)) show that placing the chine on the forebody delays the onset of instabilities that lead to vortex breakdown. This is clearly evident by comparing the moment histories from the wing/body/chine configuration (see fig. 18) with those from the wing/body configuration. The plots indicate that the moment coefficients were still oscillatory but were less random. The presence of the chine strengthens the cross-flow shock as seen in the pressure distributions (figs. 16(a)–16(d) and 17(a)–17(d)), but FLO57 does not predict this feature. Increased grid resolution may be required to capture the shock.

The lift, drag, and moment coefficient curves are given in figures 19(a)–19(c). The Euler code slightly overpredicts the increment in lift due to the chine. The induced drag was accurately predicted but the moment curve was not.

Mach 0.8 Wing/Body

With few exceptions, the trends in the computational solutions at $M_\infty = 0.8$ are similar to those at $M_\infty = 0.6$. The FLO57 pressure distributions agree well with experiment at $\alpha = 5°$ over the entire wing

because the flow is still fully attached at this condition (figs. 20(a)–20(d)). When the vortex begins to form close to the leading edge at $\alpha = 8°$, the computational pressure distributions are in poor agreement with the wind tunnel data, as shown in figures 21(a)–21(d). The pressure distributions at $\alpha = 12°$ are given in figures 22(a)–22(d). As observed at $M_\infty = 0.6$, the Euler simulation predicts bursting prematurely.

The increase in Mach number to $M_\infty = 0.8$ causes the vortex burst location to move farther forward on the wing above $\alpha = 12°$ as observed in the computational and the experimental results. The Euler solutions show poor agreement with experimental results at both $\alpha = 16°$ (figs. 23(a)–23(d)) and $\alpha = 20°$ (figs. 24(a)–24(d)). The FLO57 results do not show a distinct vortex at either angle but instead have flat spanwise pressure distributions. The moment histories in figure 25 show random behavior for both angles with a large increase in nose-down pitching moment. The lift, drag, and moment coefficient curves show good agreement until about $\alpha = 12°$ (figs. 26(a)–26(c)). As vortex bursting becomes more extensive, the Euler predictions lose their accuracy.

Mach 0.8 Wing/Body/Chine

At $M_\infty = 0.8$, as at the lower Mach number, placing the chine on the forebody above the wing surface improves the correlation between numerical and experimental results and delays the onset of bursting in both sets of data. The pressure distributions for $\alpha = 8°$, 12°, 16°, and 20° are given in figures 27(a)–27(d), 28(a)–28(d), 29(a)–29(d), and 30(a)–30(d), respectively. The moment histories for the wing/body/chine (fig. 31) are smoother than those from the wing/body case. The increase in lift and the decrease in drag from the wing/body results are overpredicted by FLO57 (figs. 32(a) and 32(b)). The shape of the moment curve was accurately predicted by the Euler code, as shown in figure 32(c).

Mach 1.2 Wing/Body

In general, the pressure correlation between the Euler and experimental results improved in supersonic flow at all angles of attack. At $\alpha = 4°$ (figs. 33(a) and 33(b)), the shape of the pressure distribution is accurately predicted. At $\alpha = 8°$ (figs. 34(a)–34(d)), the computational results show good correlation with the experimental pressures inboard of approximately 90% of the local semispan at all chordwise stations. Outboard of this location, the experimental results show a suction peak that is larger than that shown computationally. This may be attributed to poor grid resolution at the leading edge.

The computational results are accurate inboard of approximately 80% of the local semispan at $\alpha = 12°$ (see figs. 35(a)–35(d)). The experimental data show a greater pressure peak near the leading edge and a greater surface area over which the lower pressures exist. The computational velocity vectors show that a leading-edge vortex forms at about 50% of the chord. The vortex is flat and close to the surface. The fact that the vortex does not form until this point suggests that the grid density may not be sufficient to capture a weak vortex upstream of this location.

The computational results do not correlate well with experimental pressure coefficients at $\alpha = 16°$. However, the correlation tends to improve with increasing streamwise location, as shown in figures 36(a)–36(d). The experimental oil flow shows that the leading-edge vortex is stronger at $\alpha = 16°$ than at $\alpha = 12°$ and the flow is predominantly spanwise over the wing surface rather than exhibiting a strong streamwise component, as seen in figures 37 and 38. But the flow over the wing is more complicated than at the lower Mach numbers, and conclusive observations are difficult to make. The computational velocity vectors show that a leading-edge vortex does form at the apex of the wing. Also, the velocity vectors show that at supersonic Mach numbers the location of the vortex core is more inboard than at subsonic Mach numbers, and the vortex flattens and lies closer to the surface. This latter phenomenon is also seen experimentally, as described by Erickson in reference 5. Since the leading-edge vortices do not break down at the angles of attack investigated, the moment histories are stable and show that converged solutions are obtained within 1,000 iterations (see fig. 39). In addition, the moment history shows that the pitching moment becomes more stable with increasing angle of attack. This is the opposite of what is seen at the lower Mach numbers, and is to be expected, since the center of pressure moves back at supersonic speeds.

The lift, drag, and moment comparisons are given in figures 40(a)–40(c). The lift comparison shows good agreement through $\alpha = 12°$.

Mach 1.2 Wing/Body/Chine

The addition of the chine at supersonic speeds does not cause a marked improvement in the correlation between the pressures and forces that was seen at the subsonic Mach numbers. The pressure distribution is nearly identical for the wing/body and wing/body/chine configurations at $\alpha = 4°$ (figs. 41(a)–41(d)). At $\alpha = 8°$ (figs. 42(a)–42(d)) and $\alpha = 12°$ (figs. 43(a)–43(d)), the trends are similar between the two configurations, but the chine tends to increase the pressures on the upper surface. The addition of the chine brings the experimental and computational results into closer agreement at $\alpha = 16°$ (figs. 44(a)–44(d)). At $\alpha = 20°$, the comparison between the pressure distributions is not as good inboard of approximately 60% of the local semispan but does improve outboard of that location (see figs. 45(a)–45(d)). The inboard pressures computed by FLO57 are higher than the experimental pressures. The oil flow at this condition shows the existence of a cross-flow shock located between the vortex and wing upper surface which induces secondary separation as described in Ref. 5 (see fig. 46). Along the shock, there is an abrupt change in the direction of the flow on the surface. By analyzing the pressure distribution, it can be seen that the shock is not a strong one since the pressure rise is slight. This shock is not captured in the Euler solution. Secondary separation is also observed in the oil flow. In addition, the oil flow shows a small recirculation region between the location of the cross-flow shock and the tip near the trailing edge of the wing which is not captured in the Euler simulation. The moment histories show that the solutions are stable and converged within 1,000 iterations (see fig. 47). The addition of the chine causes the pitching moment to become more unstable with increasing angle of attack.

Force and moment coefficient comparisons are presented in figures 48(a)–48(c). The lift and drag show good agreement through $\alpha = 12°$.

Mach 1.4 Wing/Body/Chine

At $M_\infty = 1.4$, the suction peak at the leading edge shown previously at $M_\infty = 1.2$ has decreased in strength and size at $\alpha = 8°$ (figs. 49(a)–49(d)). The agreement between computational and experimental pressure coefficients is good. The shape and values of the pressure distribution are predicted well by the Euler code. The computed velocity vectors show that attached flow exists until $\alpha = 12°$, where a flat leading-edge vortex forms close to the upper surface. The agreement between pressure distributions at $\alpha = 12°$ degrades outboard of approximately 85% of the local semispan, where FLO57 underpredicts the expansion (see figs. 50(a)–50(d)). At $\alpha = 16°$ (figs. 51(a)–51(d)) and $\alpha = 20°$ (figs. 52(a)–52(d)), the Euler code has predicted higher pressures than those given by experiment at the 30% and 40% chord stations. The shape of the distribution and the values of the pressures are predicted accurately by FLO57 after 40% chord. The same trend in the moment history is seen at $M_\infty = 1.2$ (see fig. 53). The moment histories are stable at all angles of attack and converge within 1,000 iterations.

The force comparison between Euler and experiment shows excellent agreement at all angles of attack, as shown in figures 54(a) and 54(b). The moment correlation has improved in that the shape of the moment curve is better predicted by FLO57 than it was in the previous comparisons (fig. 54(c)).

Mach 1.6 Wing/Body/Chine

At $M_\infty = 1.6$, the shapes of the pressure distributions are accurately predicted by FLO57 at $\alpha = 4°$ (see figs. 55(a)–55(d)). At $\alpha = 8°$ (figs. 56(a)–56(d)), the suction peak shown at the lower supersonic Mach numbers has diminished even further and has disappeared aft of the 50% chord station. The correlation between FLO57 and experiment is good at the last two chord stations. The Euler results show attached flow at angles less than $\alpha = 12°$. At $\alpha = 12°$ (figs. 57(a)–57(d)), the correlation between pressures is good downstream of the 50% chord location. At the stations closer to the apex, the Euler pressures are higher than those seen in the experimental data outboard of approximately 80% of the local semispan. Inboard of this position the pressures are accurately predicted by FLO57. The correlation between pressure distributions is not as good as that at $M_\infty = 1.4$, with FLO57 predicting higher pressures than experiment at $\alpha = 16°$ (figs. 58(a)–58(d)) and $\alpha = 20°$ (figs. 59(a)–59(d)). The moment histories are shown in figure 60. The plots still show stable, converged solutions, with a destabilizing effect from increasing angle of attack.

The slope of the lift curve computed by the Euler code is slightly higher than given in the experimental results (fig. 61(a)). Also, the drag data contain a greater offset than before (fig. 61(b)). The displacement of

the moment curve has decreased, although the slope predicted by FLO57 is still too large (fig. 61(c)).

CONCLUSION

The FLO57 Euler code has been used to calculate transonic and supersonic flow solutions over two configurations of a generic fighter model. Results were computed at Mach numbers 0.6, 0.8, 1.2, 1.4, and 1.6 for angles of attack between 4° and 20°.

Although the Euler code predicts attached flow well, it is less accurate when the leading-edge vortex is just beginning to form. This may be due to the sensitivity of FLO57 to grid resolution and geometric modeling of the leading edge. For the subsonic cases, the Euler results are in good agreement with experiment until vortex breakdown occurs in the solutions. The results presented in this paper show that the Euler code tends to predict bursting prematurely. When the experimental results indicate vortex bursting, the agreement between pressure distributions improves. For the supersonic cases, vortex breakdown was not observed in the Euler solutions. Overall, the supersonic results were in better agreement with wind tunnel data than corresponding subsonic cases were.

The effect of adding the chine on the forebody was most noticeable in subsonic flow, where its addition delayed the onset of vortex breakdown both numerically and experimentally and improved the Euler predictions of the pressure distributions. The decoupled chine vortex interacts favorably with the wing flow field, and acts to increase the effective leading-edge sweep (ref. 5). The FLO57 comparisons improve with the addition of the chine because the chine fixes the forebody separation location along its leading edge and provides a dominant flow feature which the Euler code can capture. Without the chine, the Euler code cannot model the flow approaching the main wing correctly, especially at high angles of attack, because the character of the incoming flow field is largely dependent upon forebody boundary-layer separations. In supersonic flow the favorable effect of the chine is not seen, because the solutions do not show vortex breakdown at any of the angles of attack obtained with the Euler code. The main effect of the chine in supersonic flow is to push the leading-edge vortex outboard.

Ames Research Center
National Aeronautics and Space Administration
Moffett Field, CA 94035-1000, July 12, 1973

REFERENCES

1. Newsome, R. W.; and Kandil, O. A.: Vortical Flow Aerodynamics — Physical Aspects and Numerical Simulation. AIAA Paper 87-0205, Jan. 1987.

2. Erickson, G. E.; and Rogers, L. W.: Experimental Study of the Vortex Flow Behavior on a Generic Fighter Wing at Subsonic and Transonic Speeds. AIAA Paper 87-1262, Jan. 1987.

3. Stanbrook, A.; and Squire, L. C.: Possible Types of Flow at Swept Leading Edges. Aeronautical Quarterly, vol. XV, pt. 1, Feb. 1964, pp. 72–82.

4. Miller, D. S.; and Wood, R. M.: Lee-Side Flow Over Delta Wings at Supersonic Speeds. NASA TP-2430, 1985.

5. Erickson, G. E.; Rogers, L. W.; Schreiner, J. A.; and Lee, D. G.: Subsonic and Transonic Vortex Aerodynamics of a Generic Forebody Strake-Cropped Delta Wing Fighter. AIAA Paper 88-2596, June 1988.

6. Powell, K. G.: Vortical Solutions of the Conical Euler Equations. Ph.D. Thesis, Massachusetts Institute of Technology, 1987.

7. Fujii, K.; and Schiff, L. B.: Numerical Simulation of Vortical Flows Over a Strake-Delta Wing. AIAA Paper 87-1229, 1987.

8. Powell, K. G.; Murman, E. M.; Perez, E.; and Baron, J.: Total Pressure Loss in Vortical Solutions of the Conical Euler Equations. AIAA Paper 85-1701, July 1985.

9. Jameson, A.; and Baker, T. J.: Solution of the Euler Equations for Complex Configurations. AIAA Paper 83-1929CP, in AIAA Computational Fluid Dynamics Conference proceedings, 1983.

10. Goodsell, A. M.; Madson, M. D.; and Melton, J. E.: TranAir and Euler Computations of a Generic Fighter Including Comparisons with Experimental Data. AIAA Paper 89-0263, Jan. 1989.

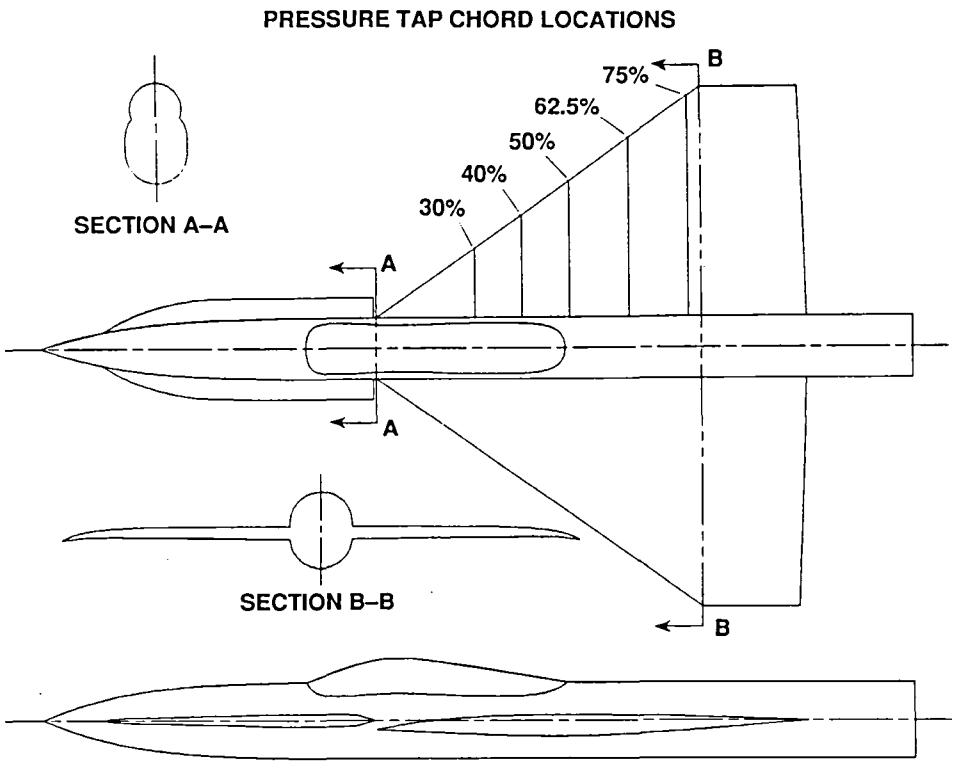

Figure 1. Generic fighter with chine.

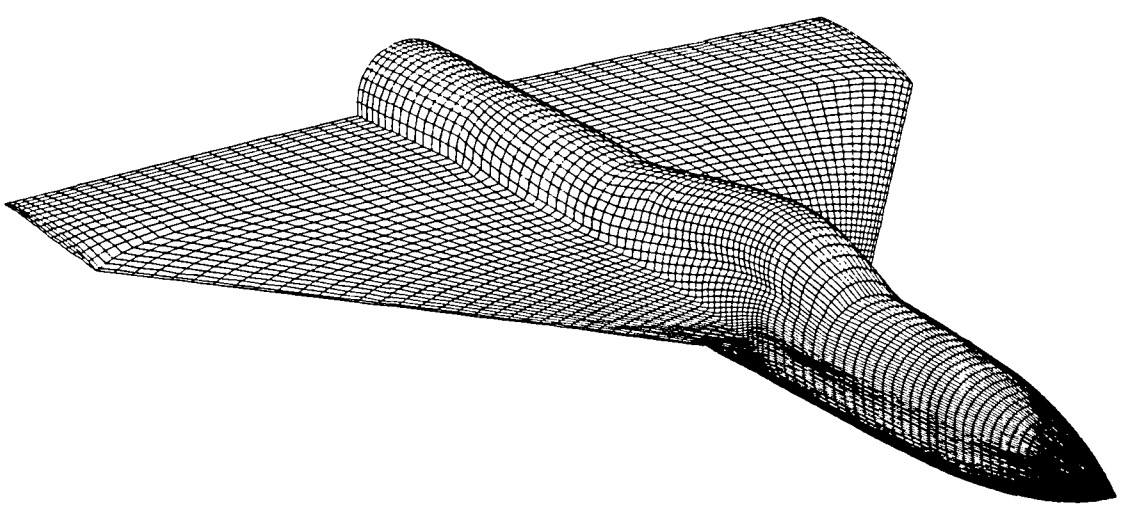

Figure 2. Generic fighter wing/body surface grid, 134 × 49 × 65 points.

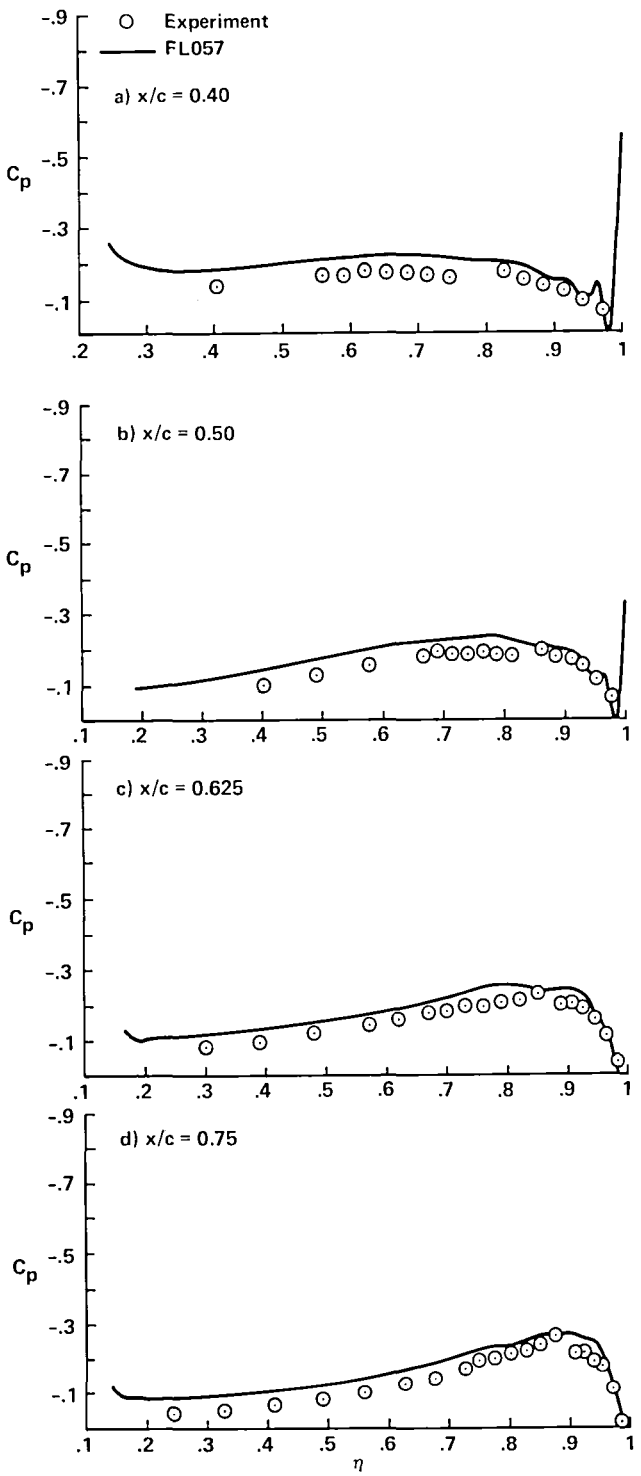

Figure 3. Upper surface pressure distributions for wing/body; $M_\infty = 0.6$, $\alpha = 4.0°$.

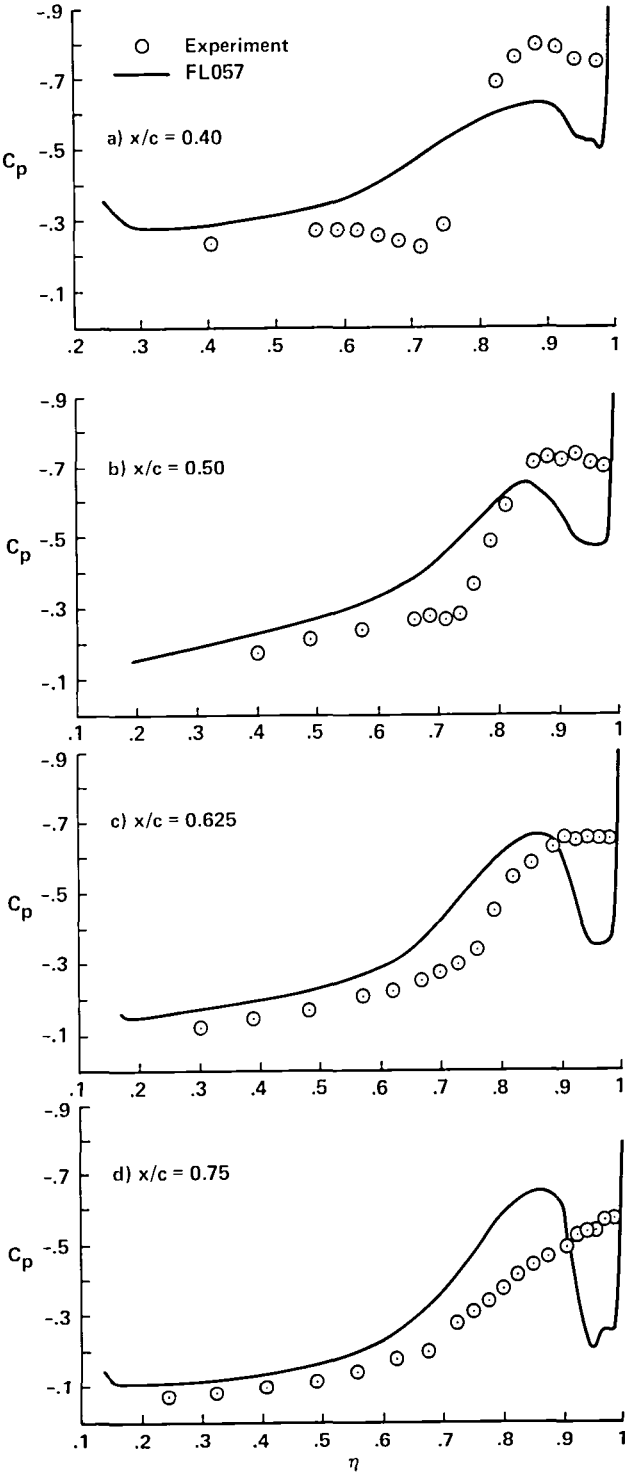

Figure 4. Upper surface pressure distributions for wing/body; $M_\infty = 0.6$, $\alpha = 8.0°$.

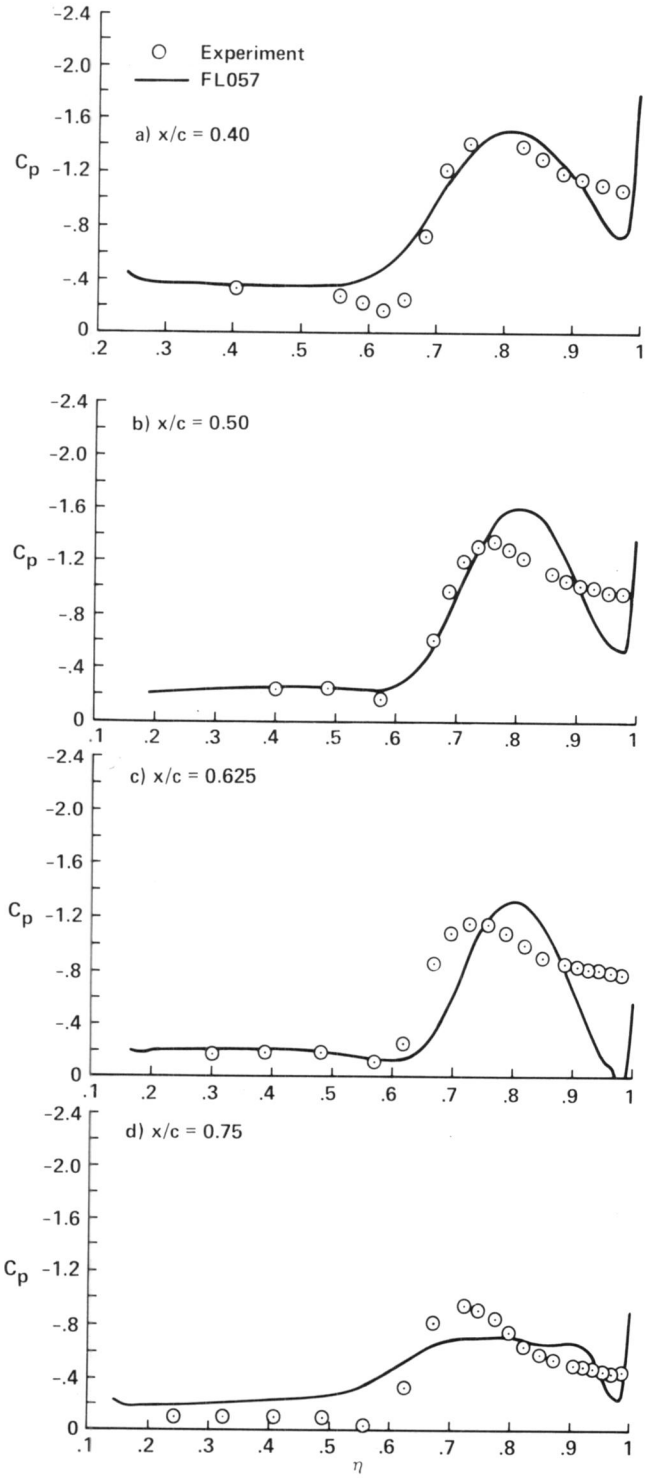

Figure 5. Upper surface pressure distributions for wing/body; $M_\infty = 0.6$, $\alpha = 12.0°$.

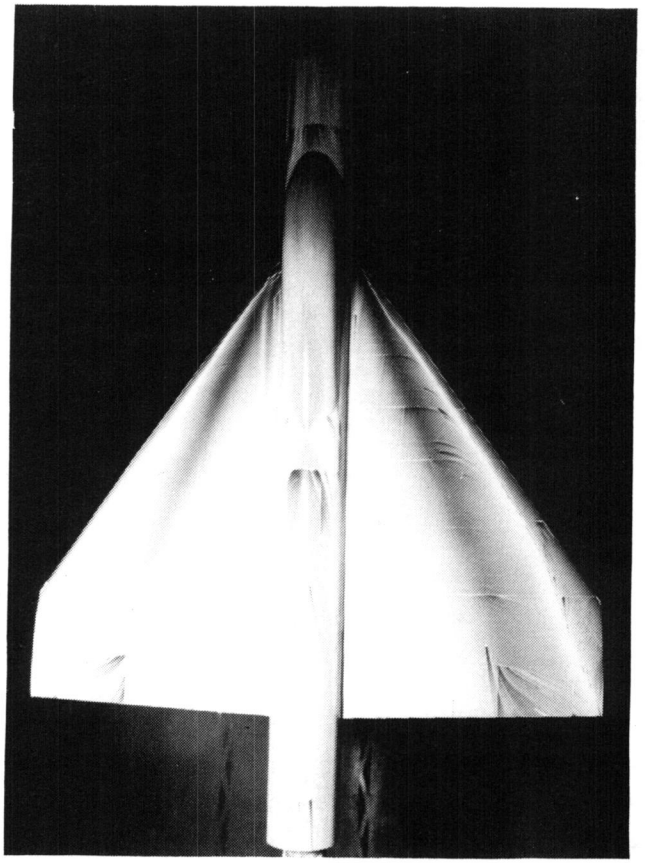

Figure 6. Oil flow visualization of wing/body; $M_\infty = 0.6$, $\alpha = 12.0°$.

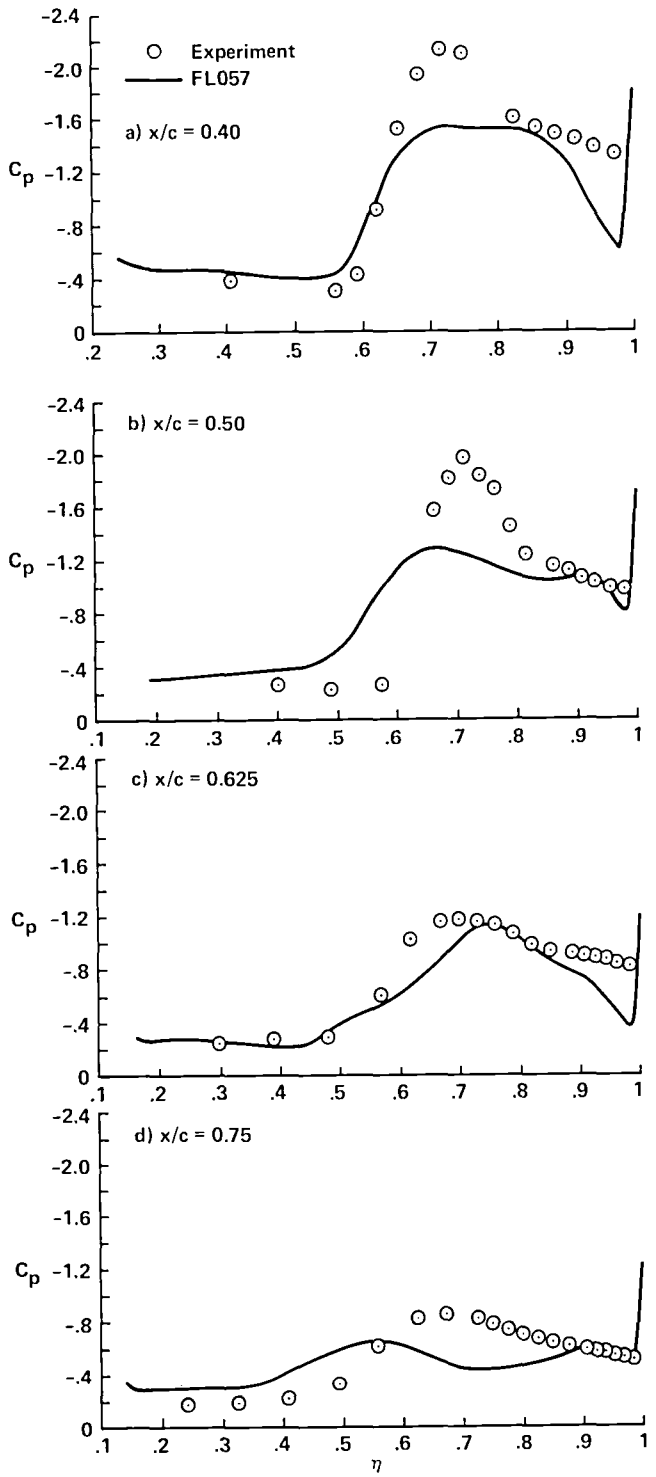

Figure 7. Upper surface pressure distributions for wing/body; $M_\infty = 0.6$, $\alpha = 16.0°$.

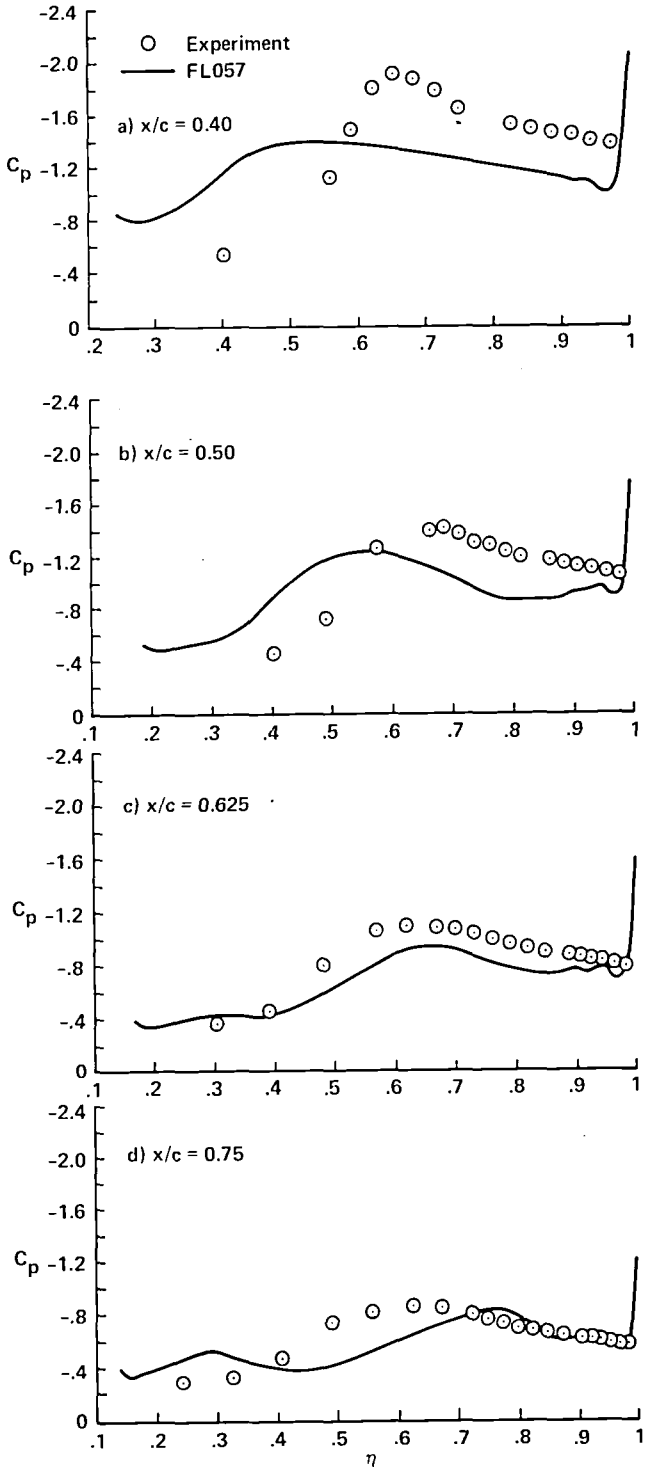

Figure 8. Upper surface pressure distributions for wing/body; $M_\infty = 0.6$, $\alpha = 20.0°$.

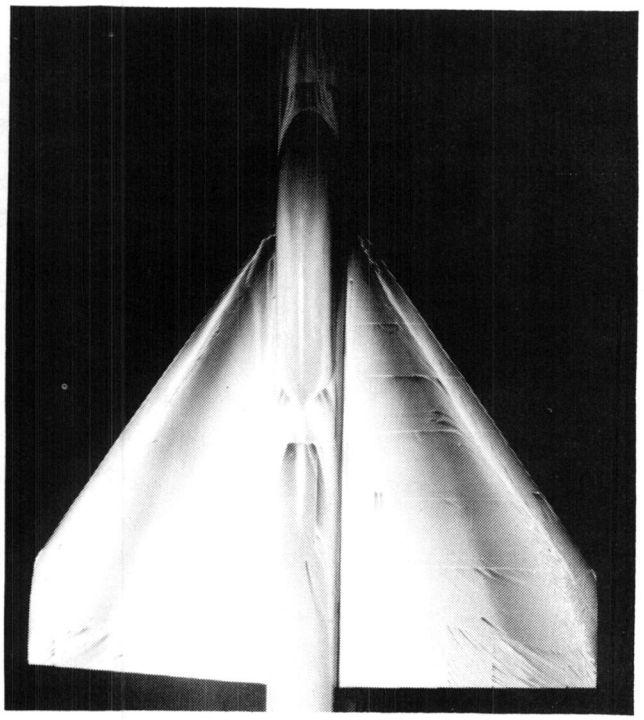

Figure 9. Oil flow visualization of wing/body; $M_\infty = 0.6$, $\alpha = 16.0°$.

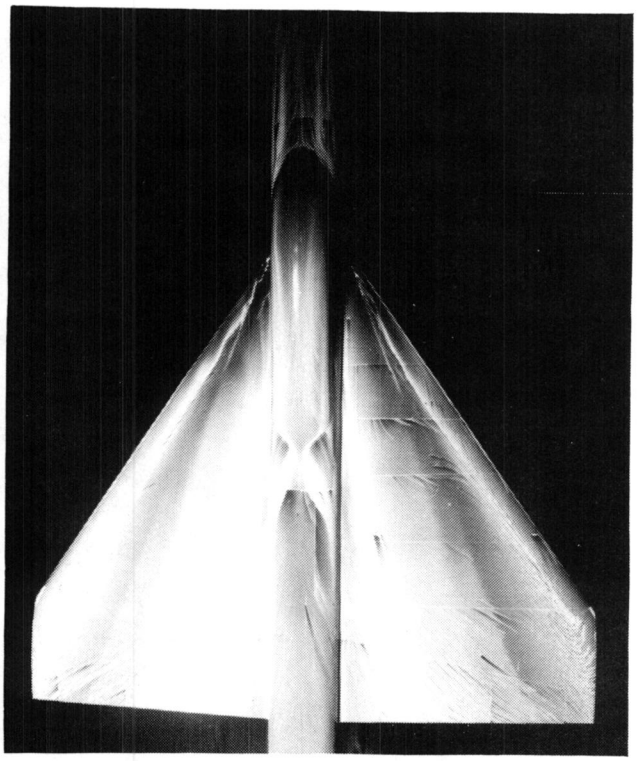

Figure 10. Oil flow visualization of wing/body; $M_\infty = 0.6$, $\alpha = 20.0°$.

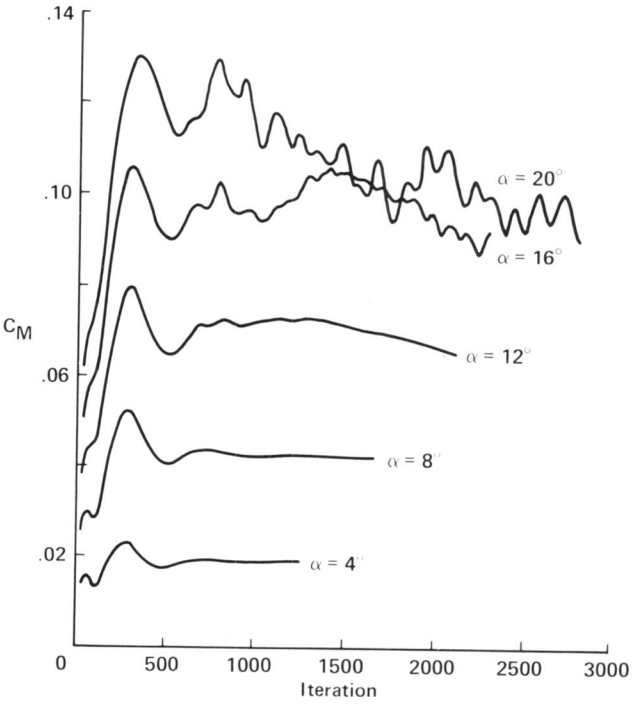

Figure 11. Pitching moment history for wing/body, $M_\infty = 0.6$.

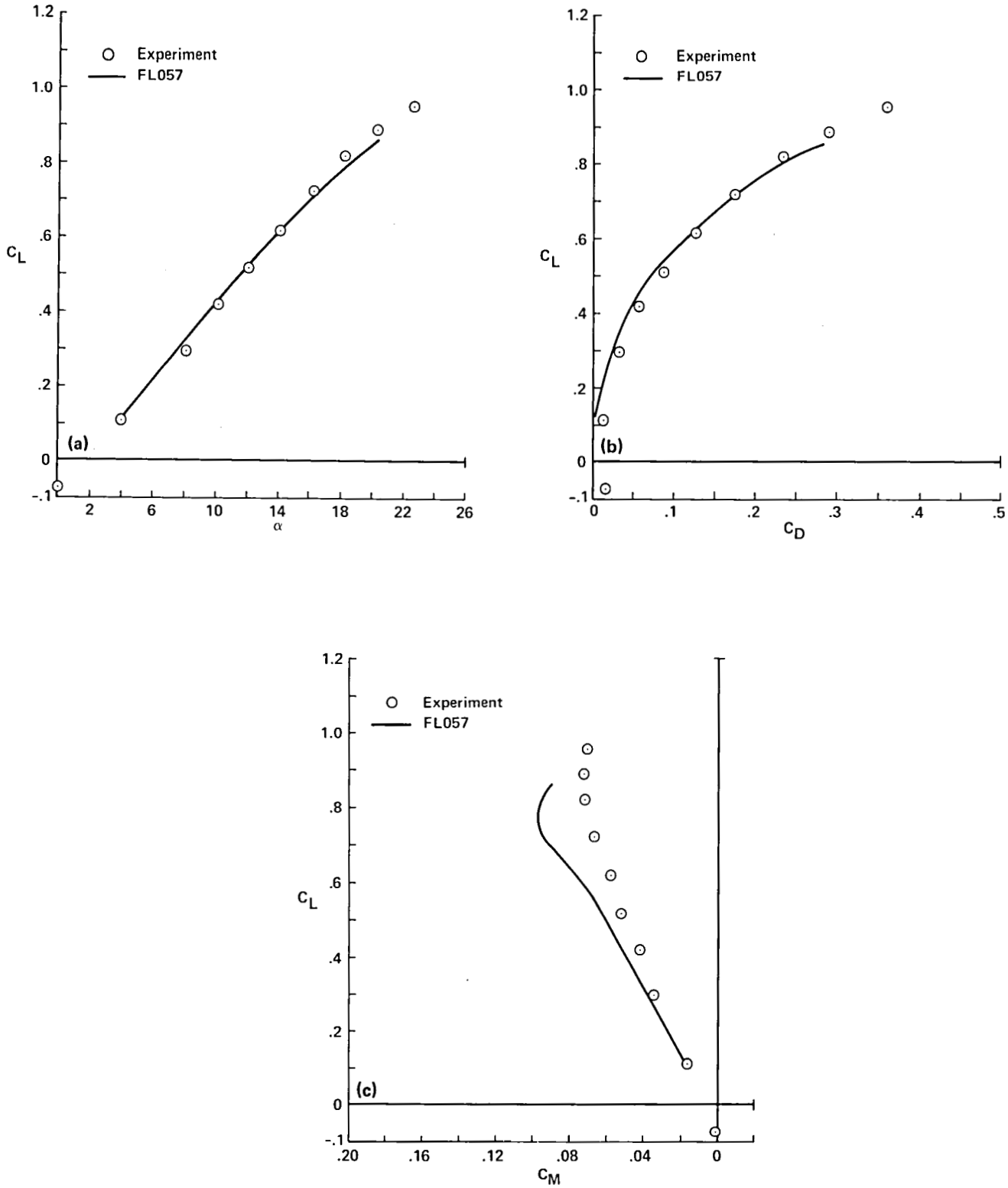

Figure 12. Experiment–CFD forces and moments for wing/body, $M_\infty = 0.6$; (a) lift curve, (b) drag polar, (c) moment curve.

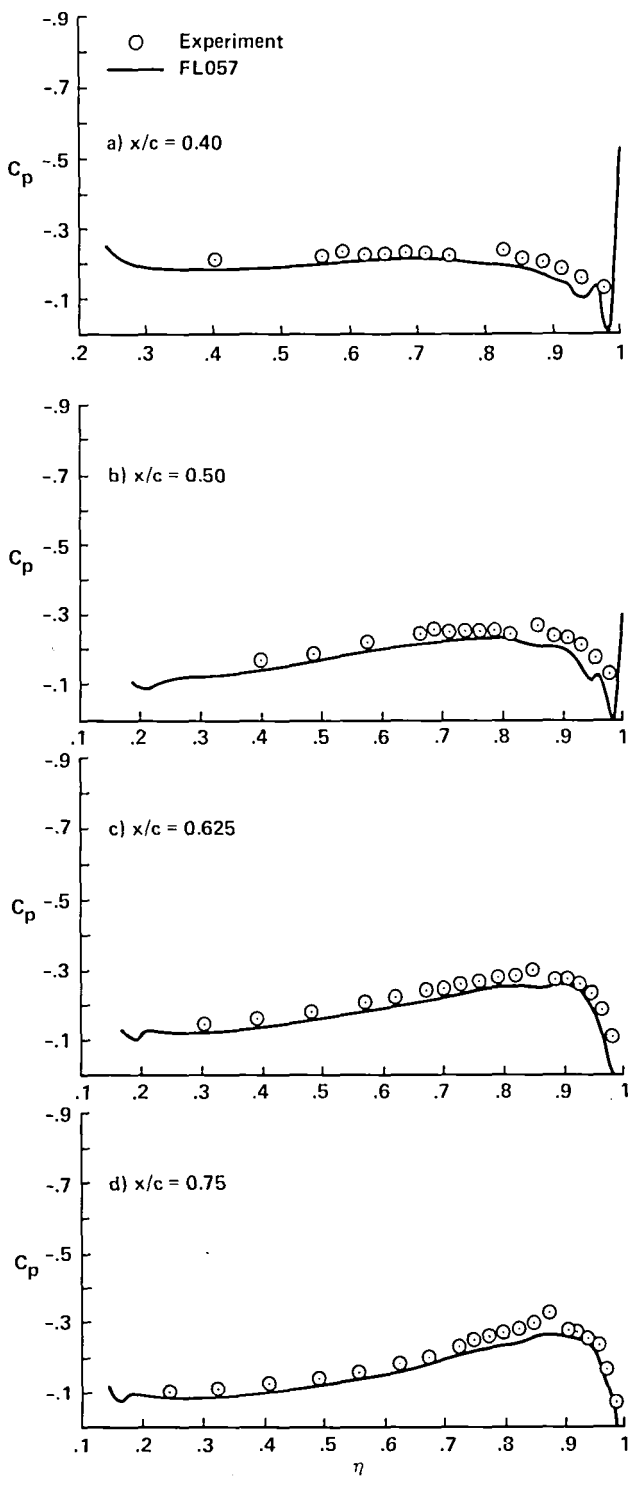

Figure 13. Upper surface pressure distributions for wing/body/chine; $M_\infty = 0.6$, $\alpha = 4.0°$.

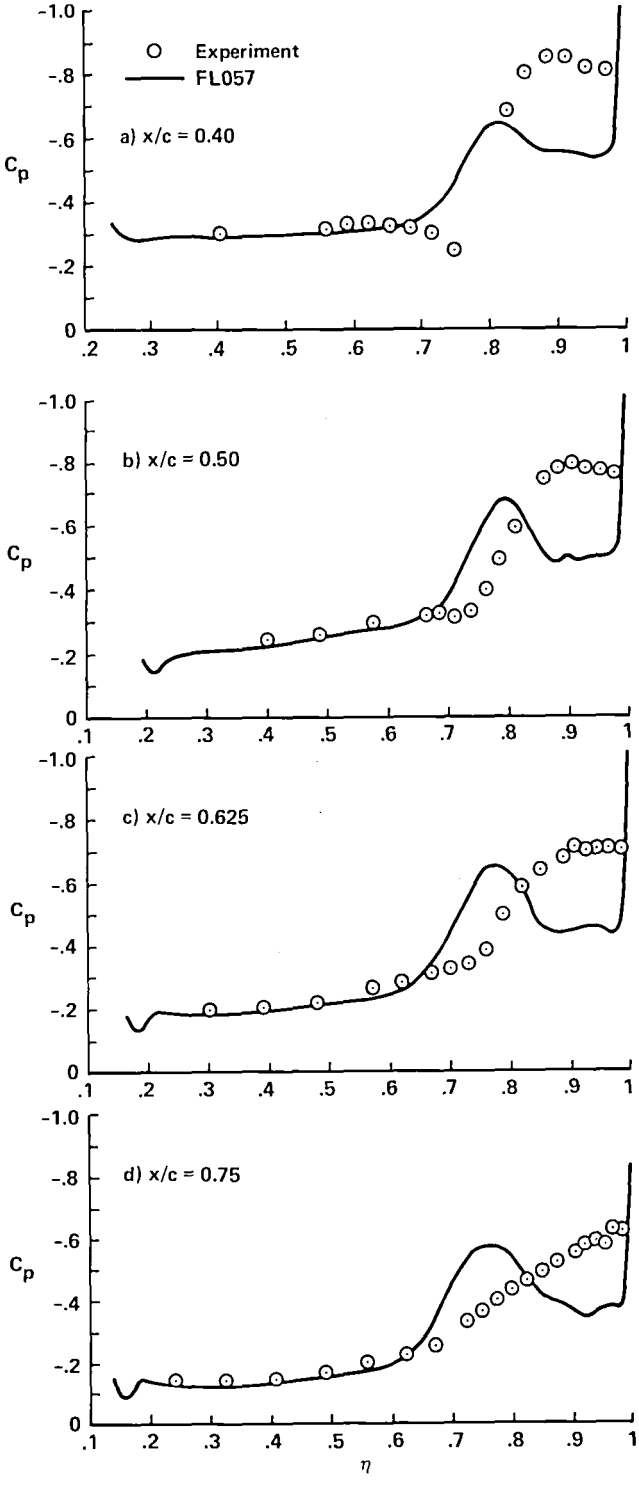

Figure 14. Upper surface pressure distributions for wing/body/chine; $M_\infty = 0.6$, $\alpha = 8.0°$.

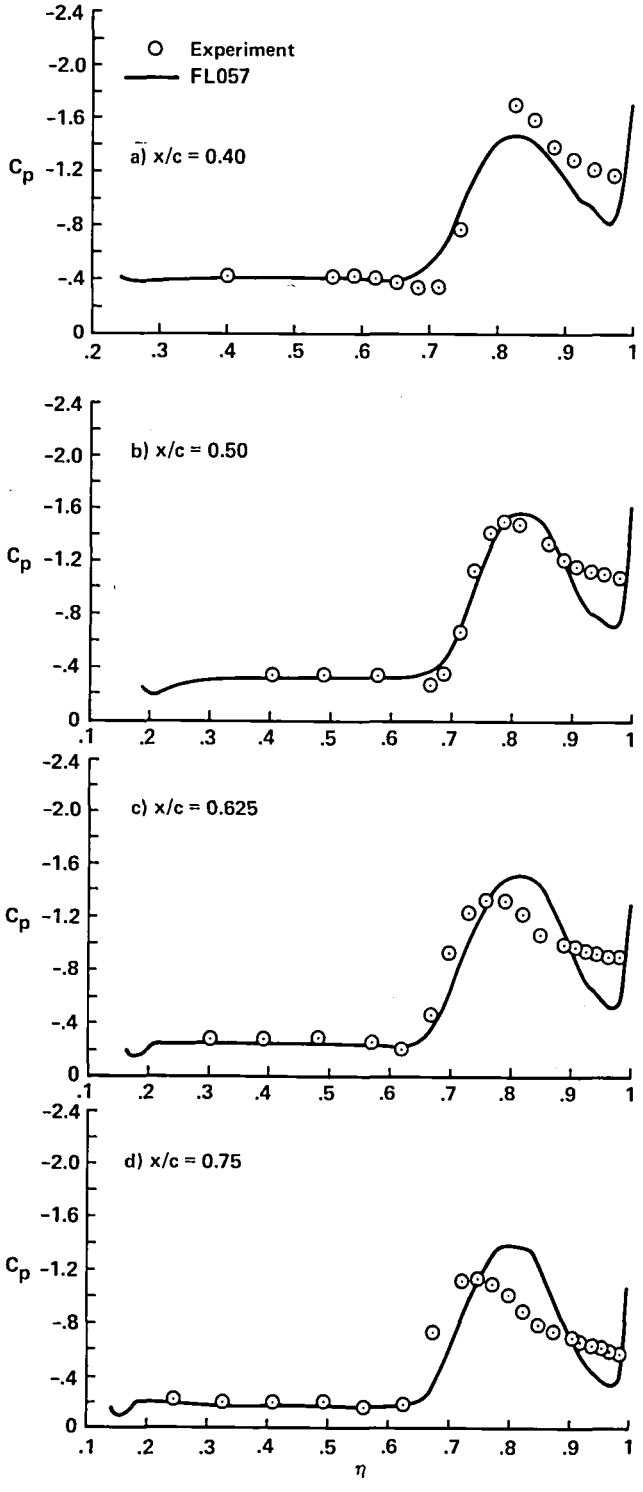

Figure 15. Upper surface pressure distributions for wing/body/chine; $M_\infty = 0.6$, $\alpha = 12.0°$.

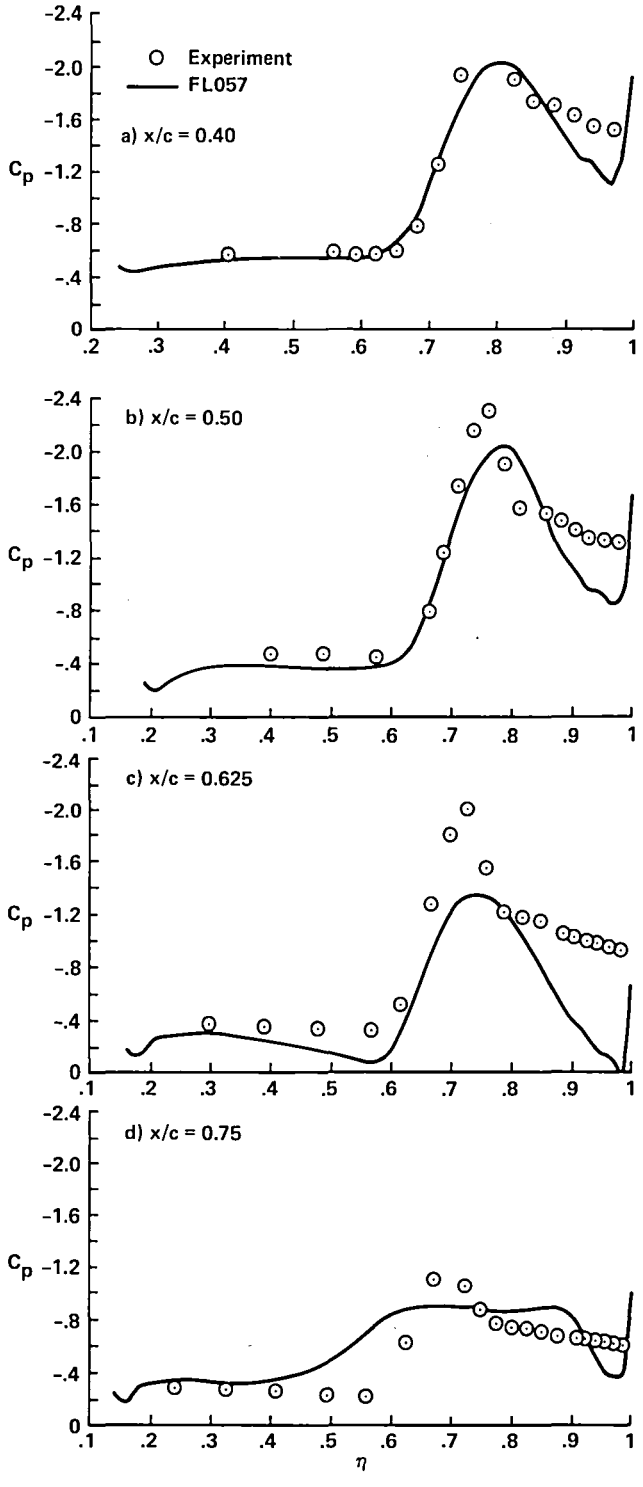

Figure 16. Upper surface pressure distributions for wing/body/chine; $M_\infty = 0.6$, $\alpha = 16.0°$.

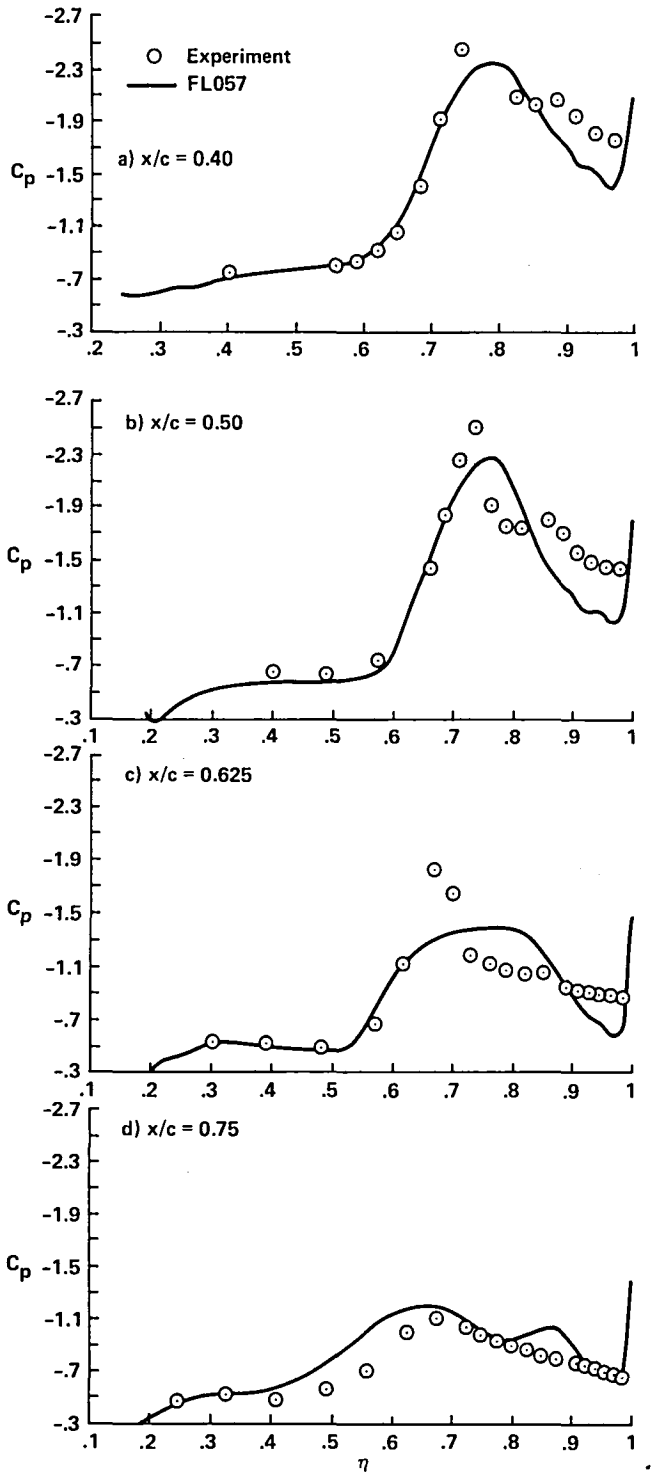

Figure 17. Upper surface pressure distributions for wing/body/chine; $M_\infty = 0.6$, $\alpha = 20.0°$.

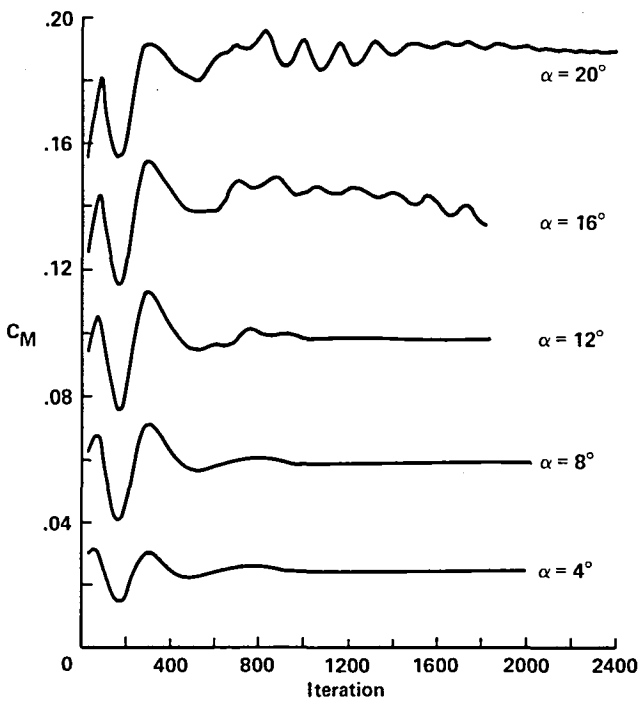

Figure 18. Pitching moment history for wing/body/chine, $M_\infty = 0.6$.

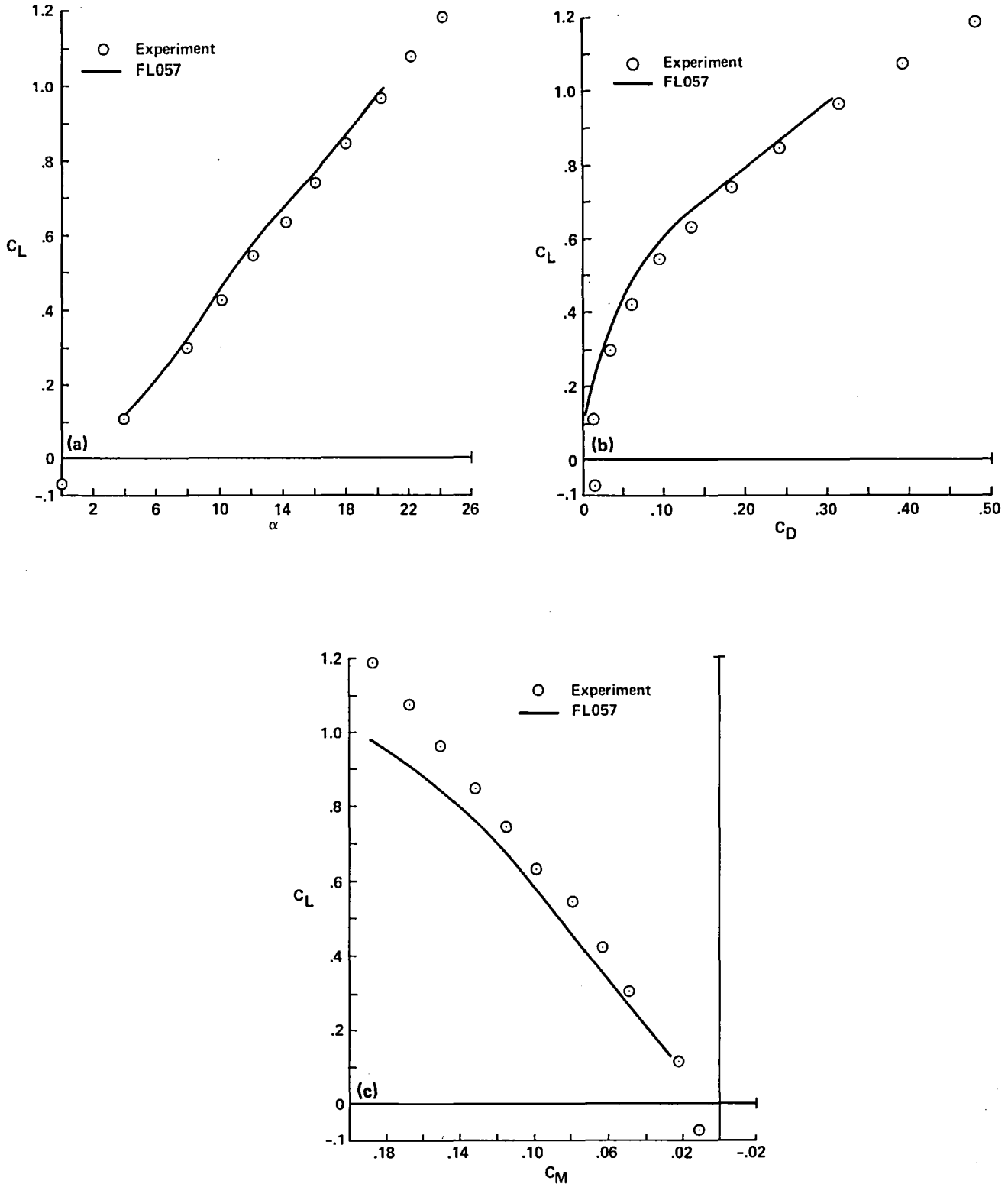

Figure 19. Experiment–CFD forces and moments for wing/body/chine, $M_\infty = 0.6$; (a) lift curve, (b) drag polar, (c) moment curve.

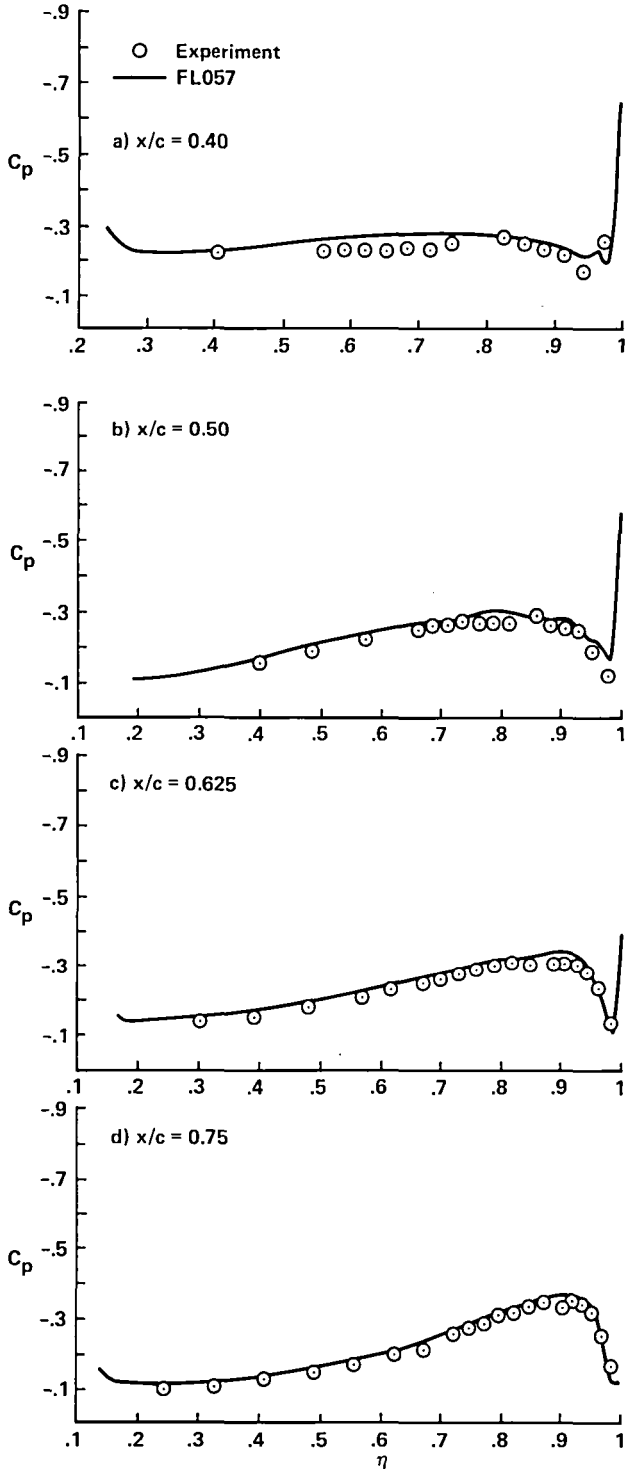

Figure 20. Upper surface pressure distributions for wing/body; $M_\infty = 0.8$, $\alpha = 5.0°$.

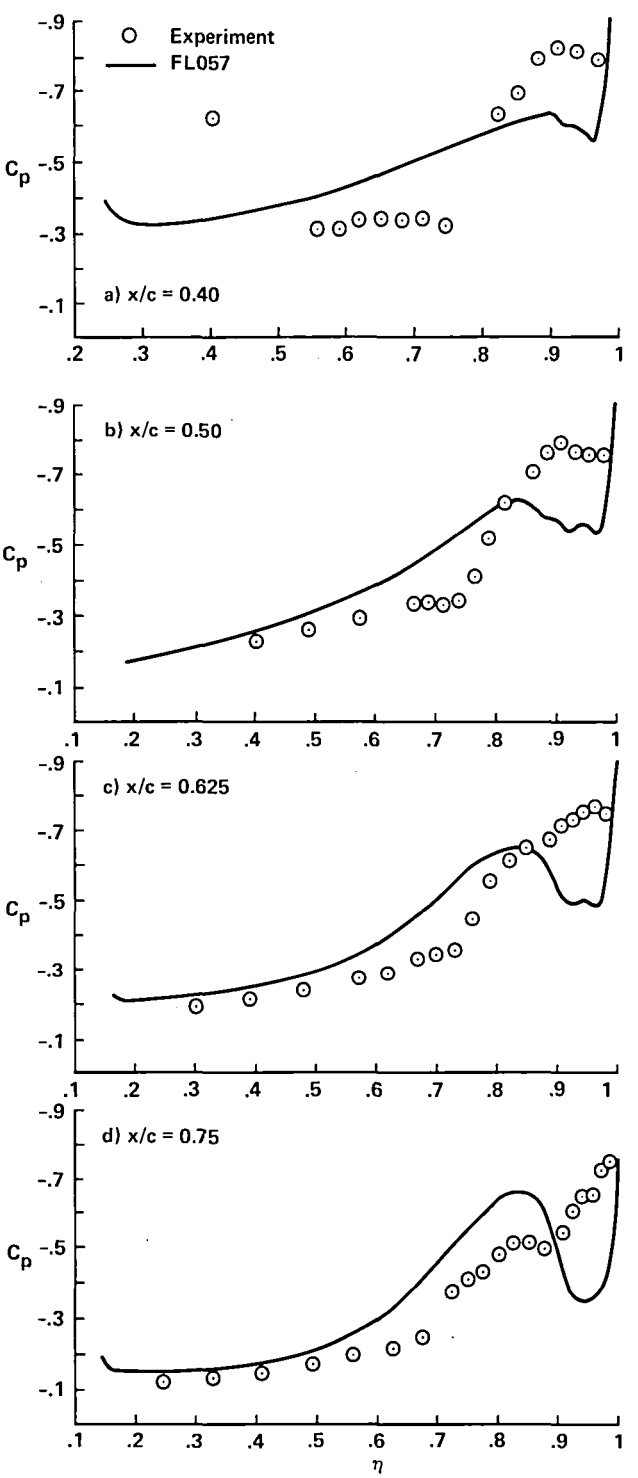

Figure 21. Upper surface pressure distributions for wing/body; $M_\infty = 0.8$, $\alpha = 8.0°$.

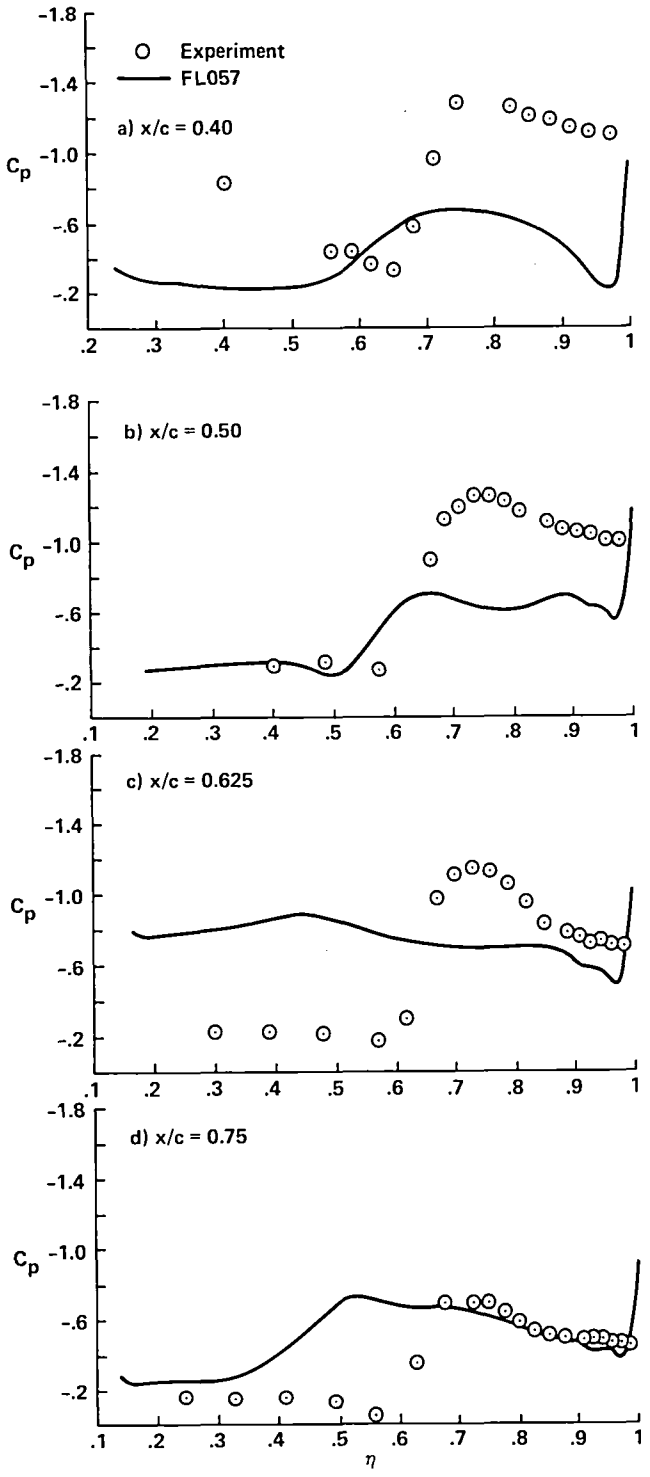

Figure 22. Upper surface pressure distributions for wing/body; $M_\infty = 0.8$, $\alpha = 12.0°$.

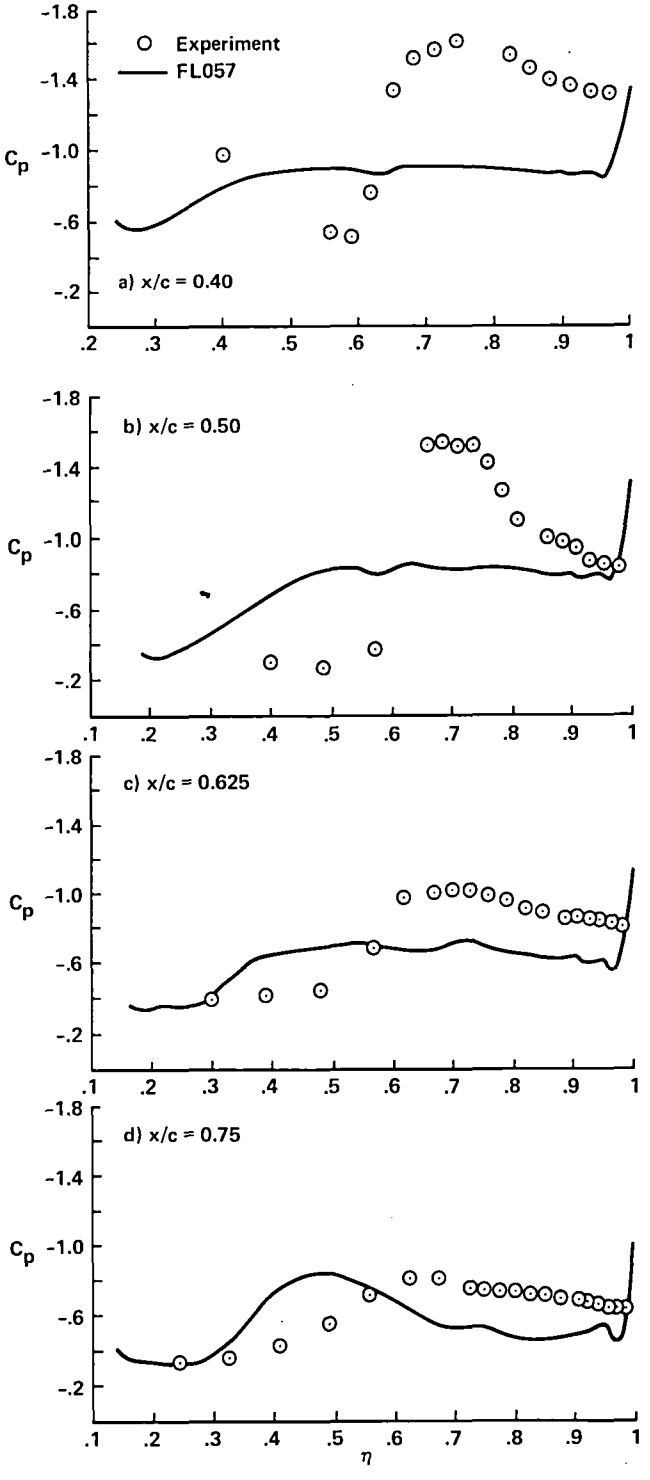

Figure 23. Upper surface pressure distributions for wing/body; $M_\infty = 0.8$, $\alpha = 16.0°$.

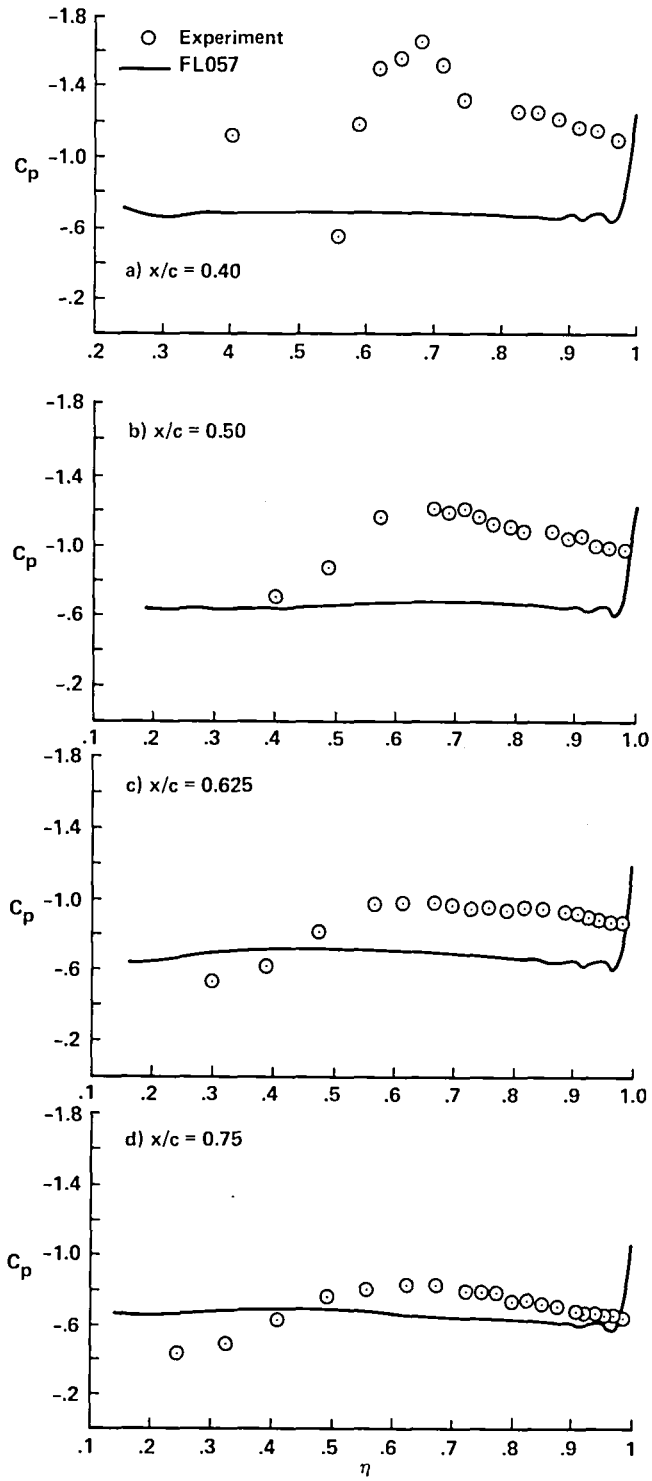

Figure 24. Upper surface pressure distributions for wing/body; $M_\infty = 0.8$, $\alpha = 20.0°$.

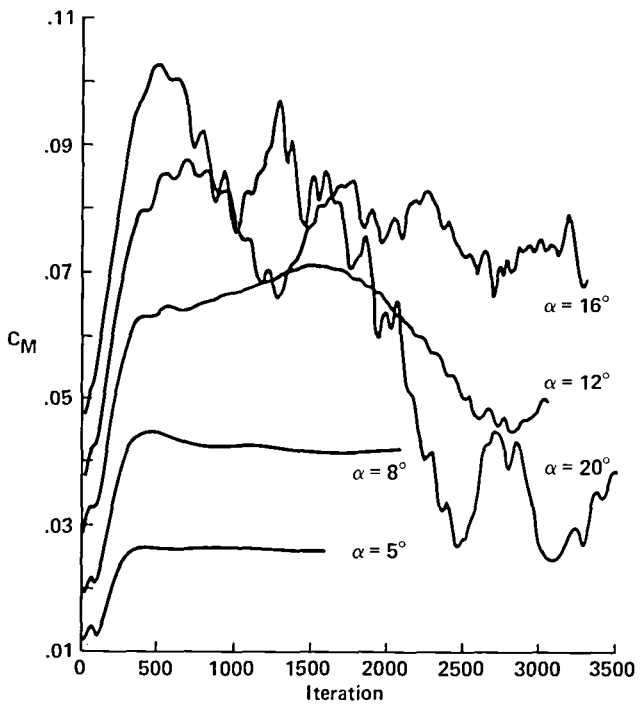

Figure 25. Pitching moment history for wing/body, $M_\infty = 0.8$.

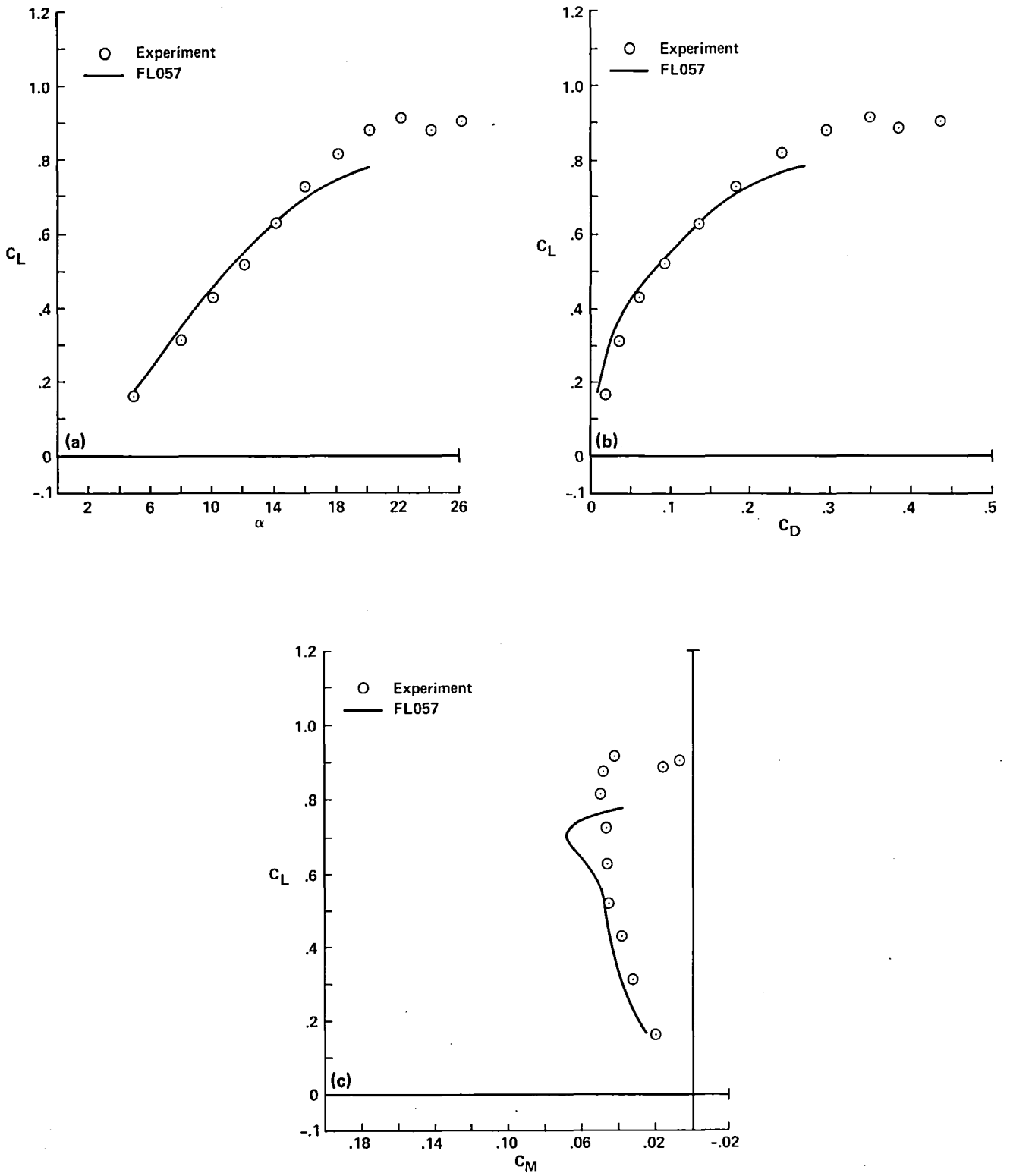

Figure 26. Experiment–CFD forces and moments for wing/body, $M_\infty = 0.8$; (a) lift curve, (b) drag polar, (c) moment curve.

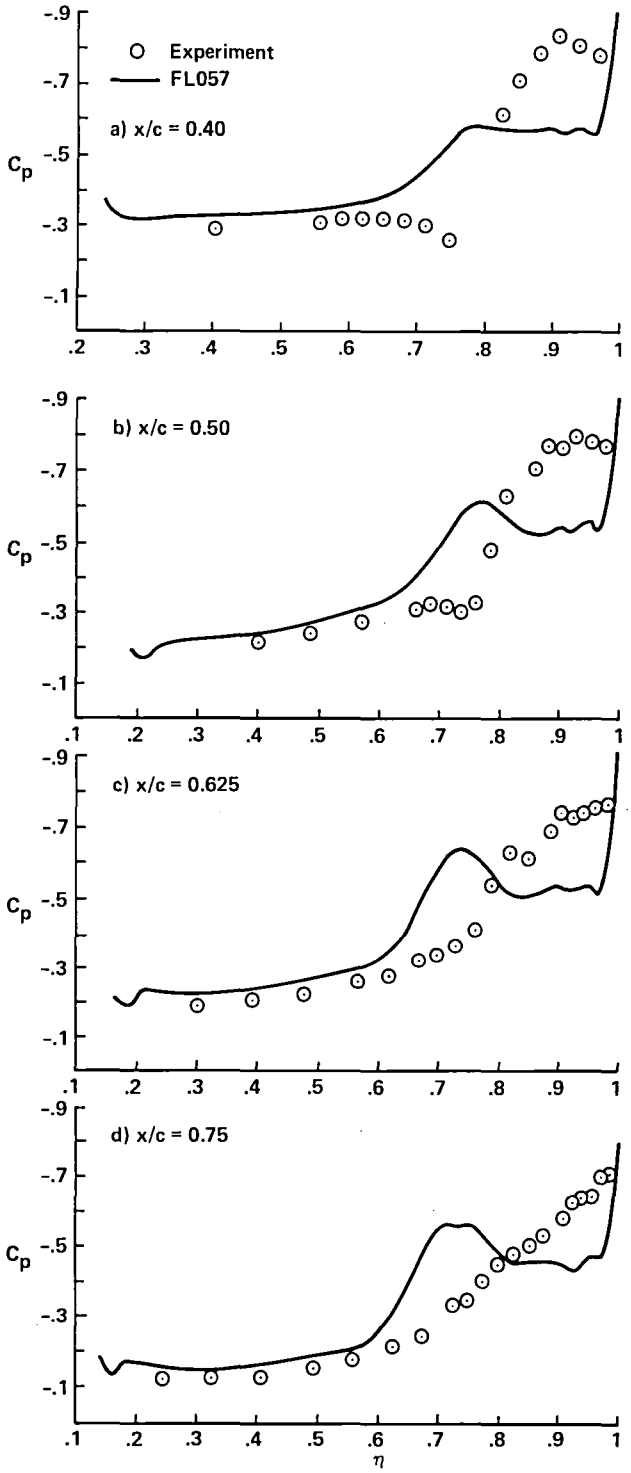

Figure 27. Upper surface pressure distributions for wing/body/chine; $M_\infty = 0.8$, $\alpha = 8.0°$.

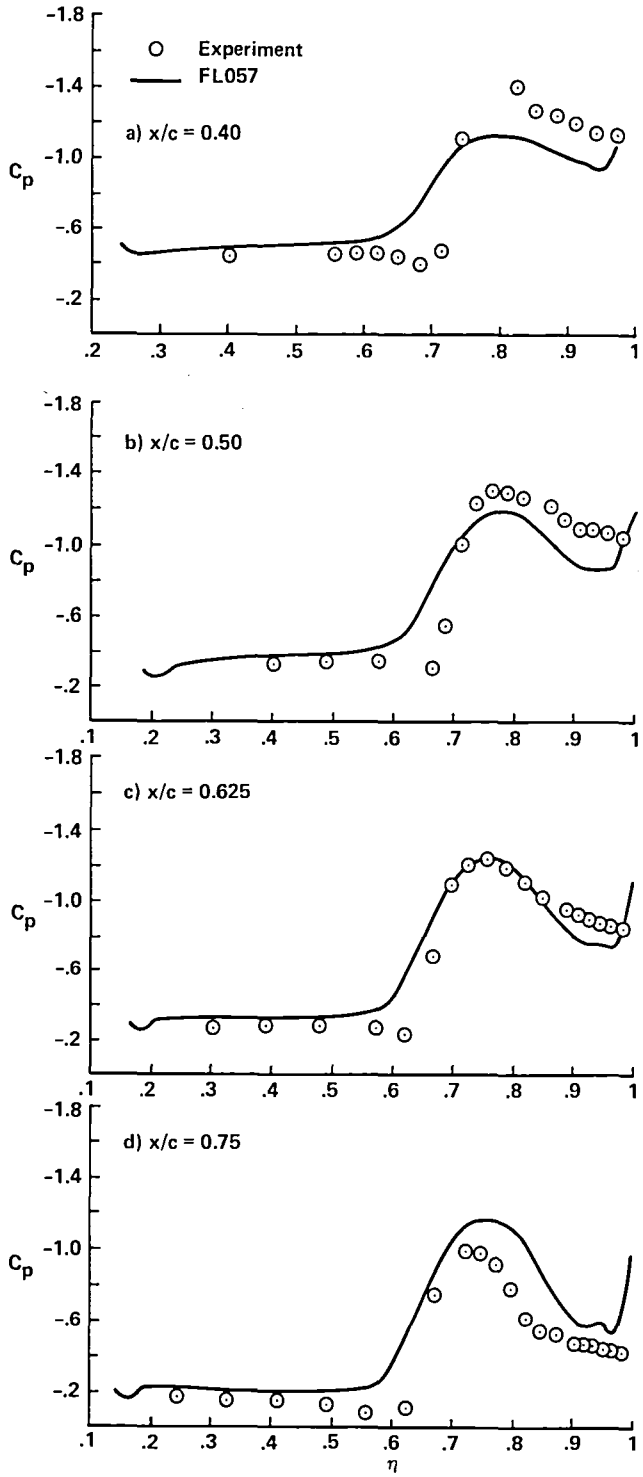

Figure 28. Upper surface pressure distributions for wing/body/chine; $M_\infty = 0.8$, $\alpha = 12.0°$.

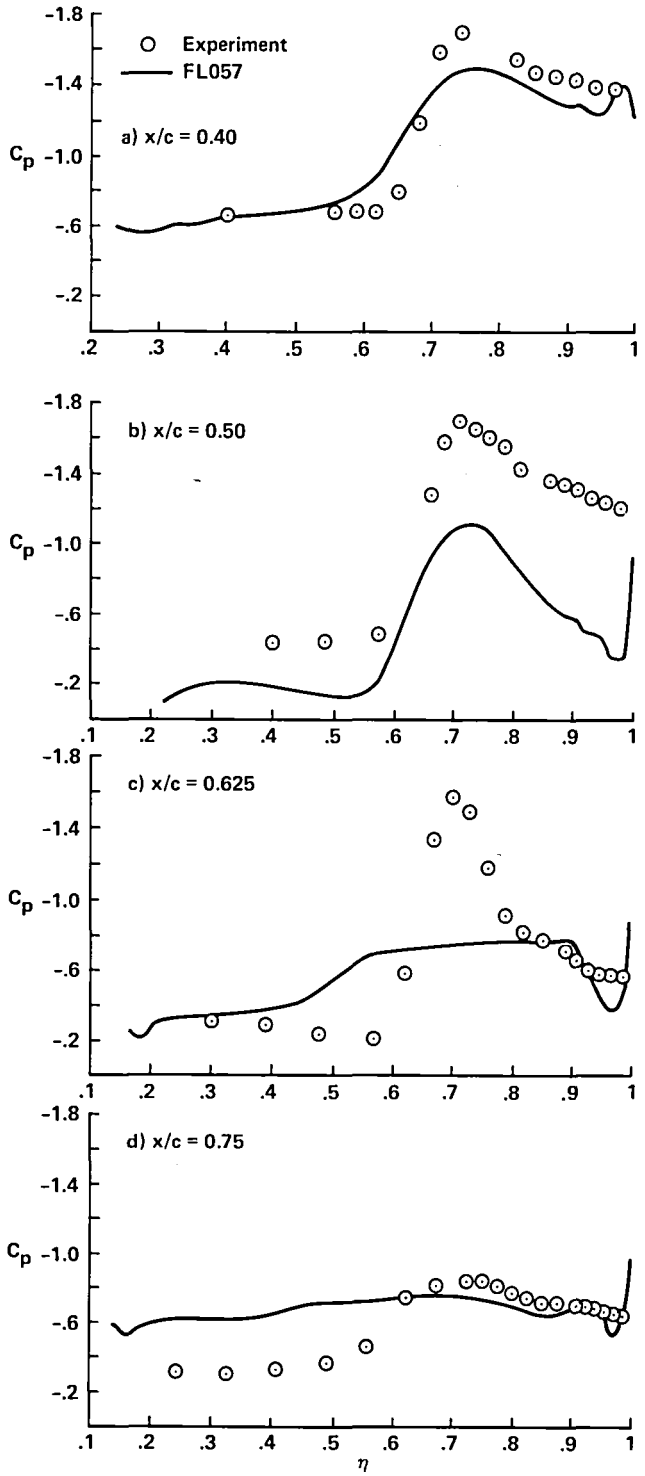

Figure 29. Upper surface pressure distributions for wing/body/chine; $M_\infty = 0.8$, $\alpha = 16.0°$.

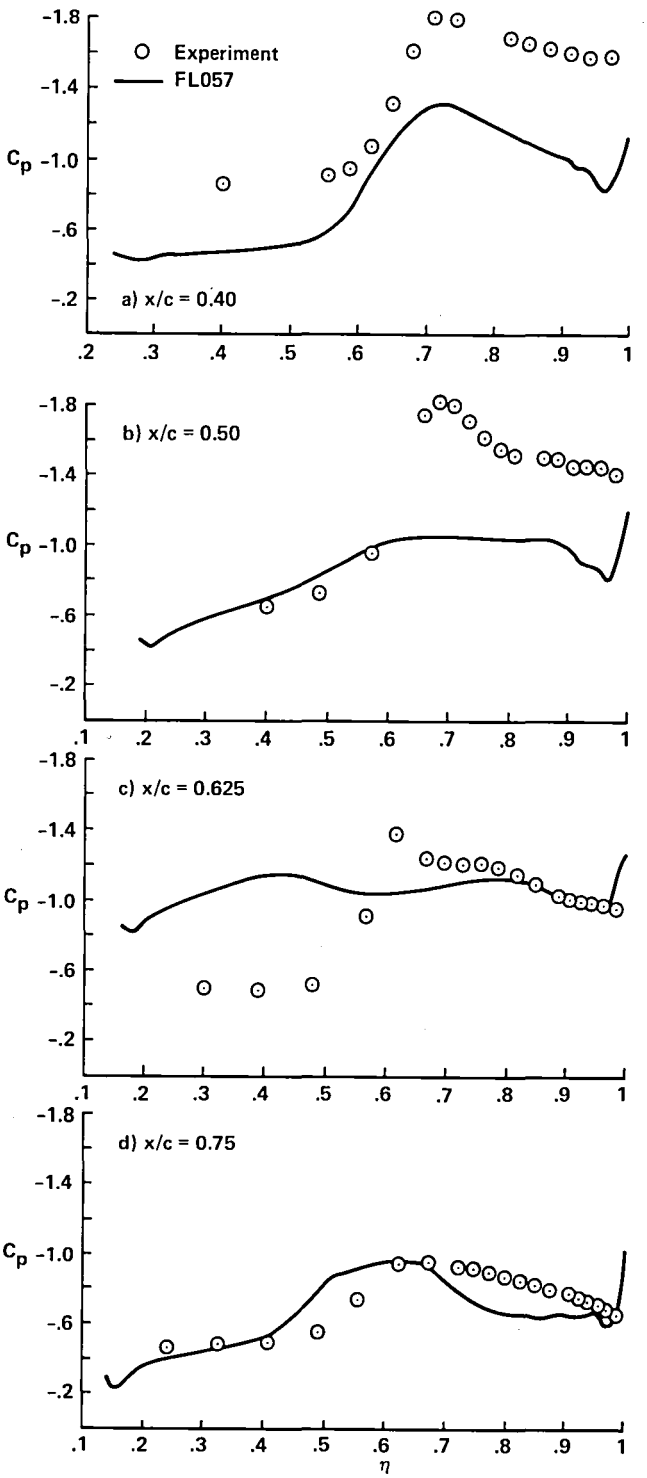

Figure 30. Upper surface pressure distributions for wing/body/chine; $M_\infty = 0.8$, $\alpha = 20.0°$.

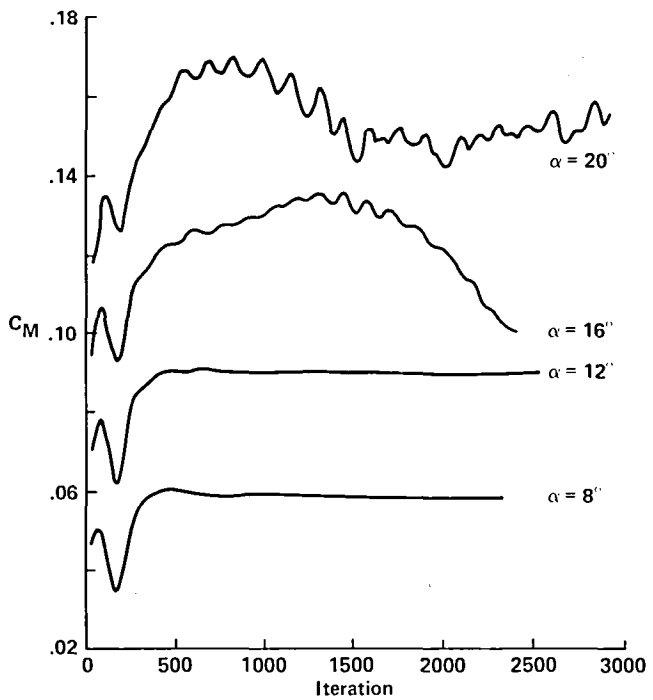

Figure 31. Pitching moment history for wing/body/chine, $M_\infty = 0.8$.

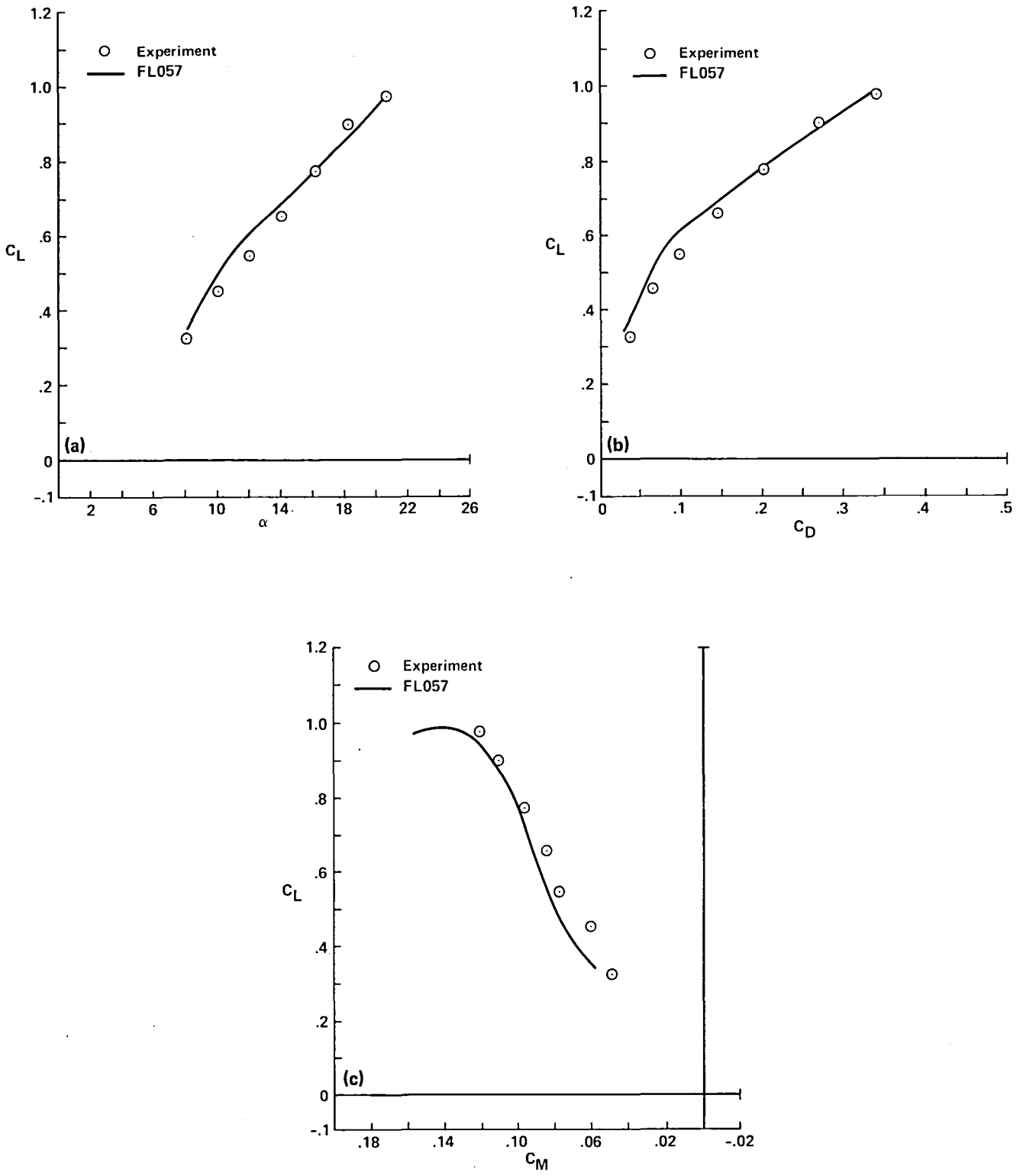

Figure 32. Experiment–CFD forces and moments for wing/body/chine, $M_\infty = 0.8$; (a) lift curve, (b) drag polar, (c) moment curve.

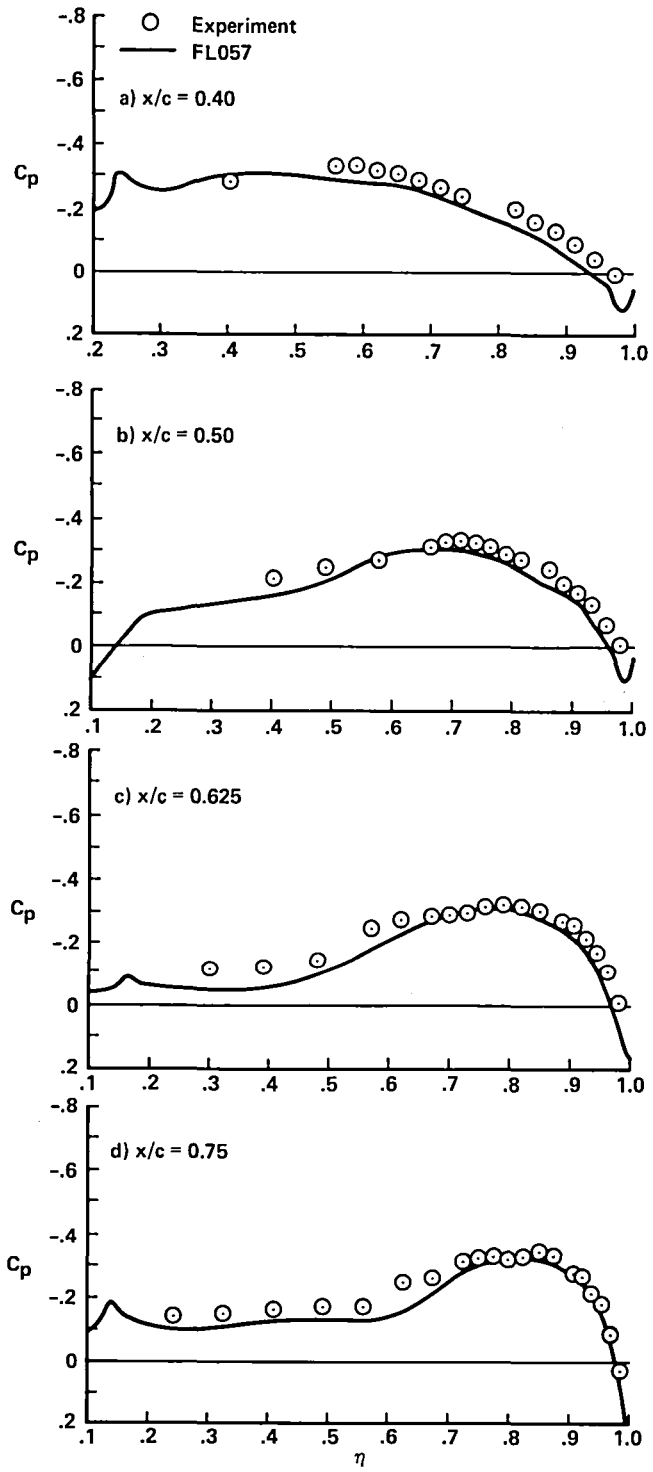

Figure 33. Upper surface pressure distributions for wing/body; $M_\infty = 1.2$, $\alpha = 4.0°$.

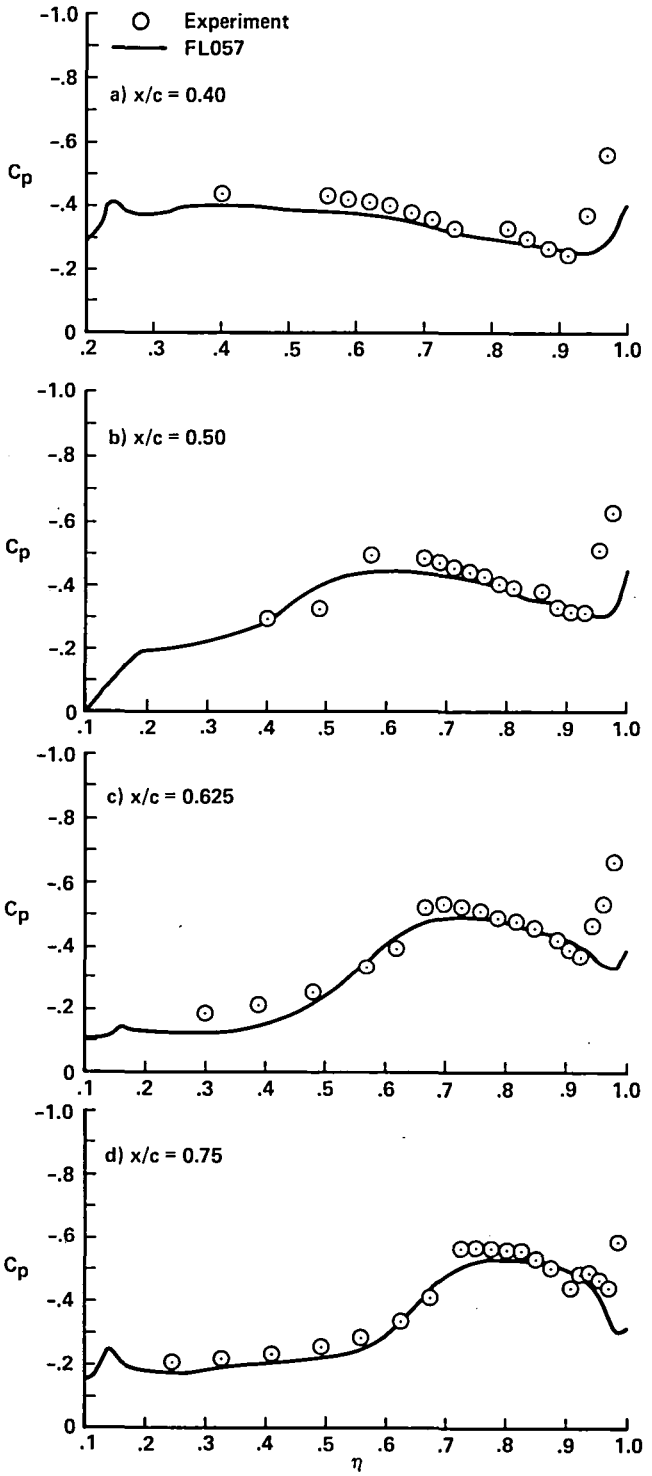

Figure 34. Upper surface pressure distributions for wing/body; $M_\infty = 1.2$, $\alpha = 8.0°$.

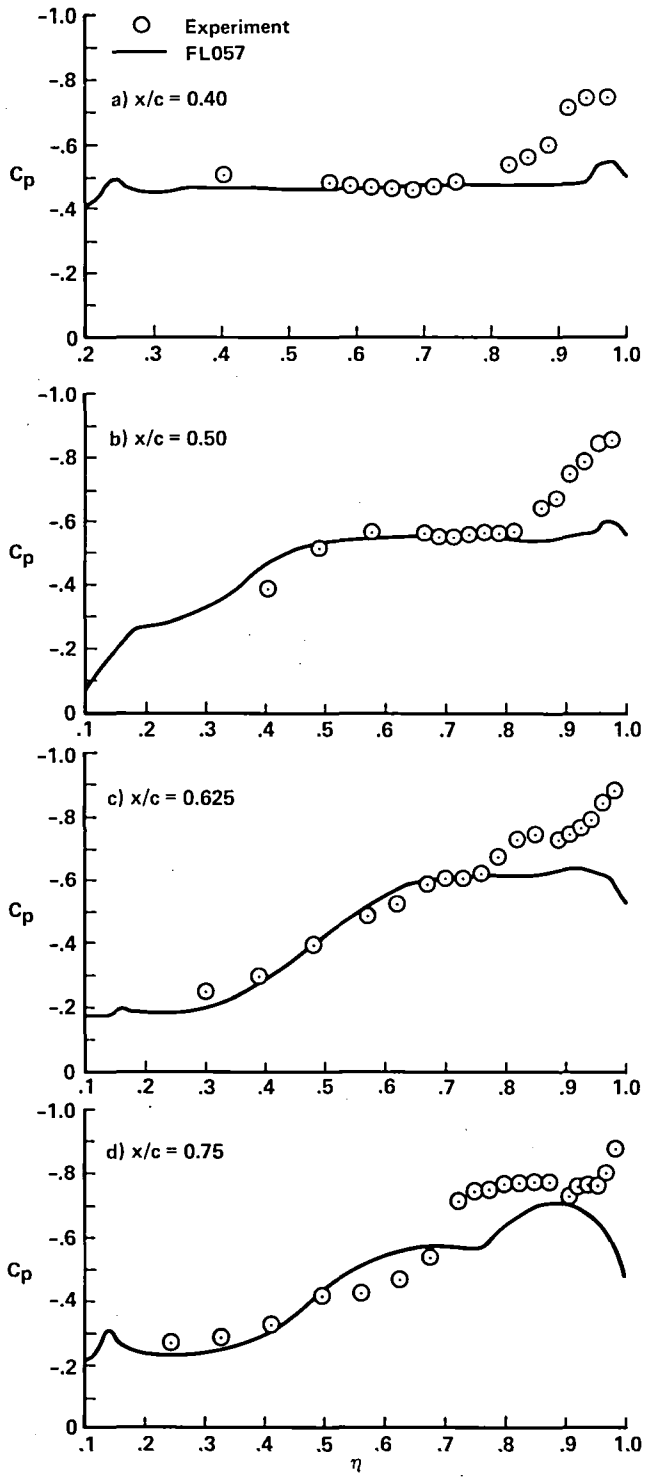

Figure 35. Upper surface pressure distributions for wing/body; $M_\infty = 1.2$, $\alpha = 12.0°$.

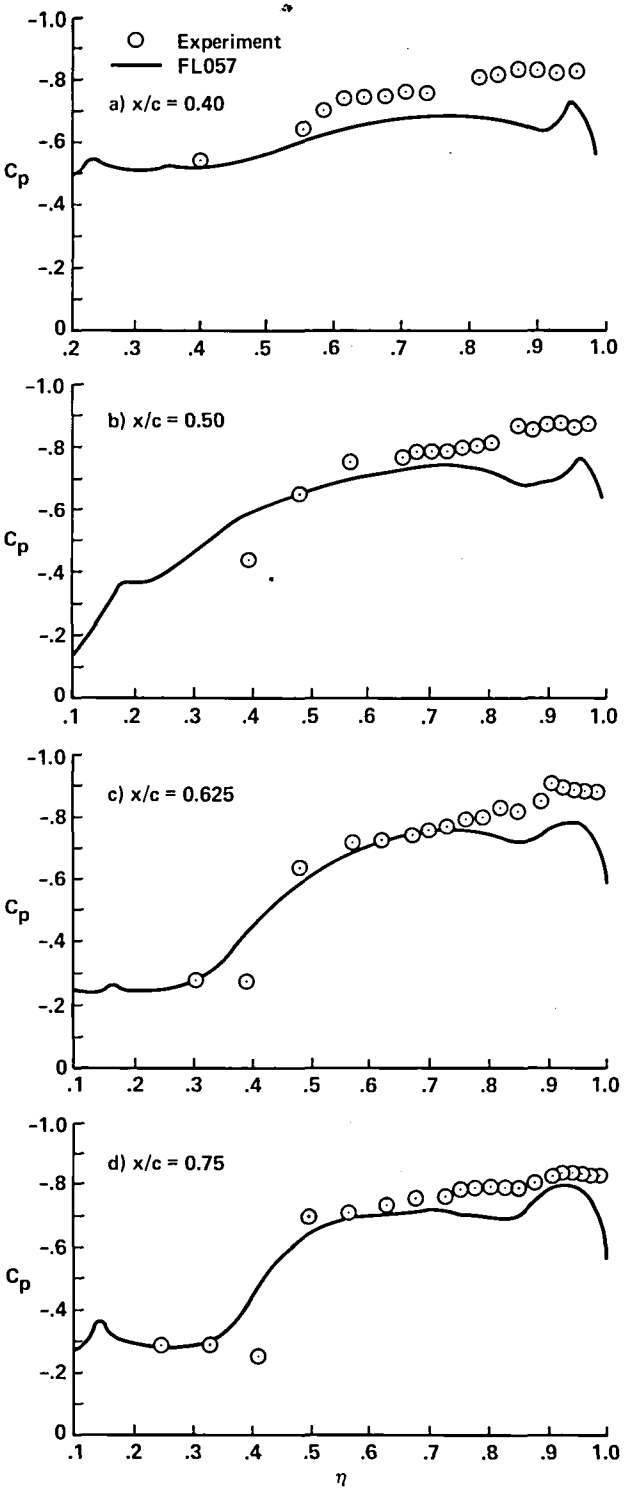

Figure 36. Upper surface pressure distributions for wing/body; $M_\infty = 1.2$, $\alpha = 16.0°$.

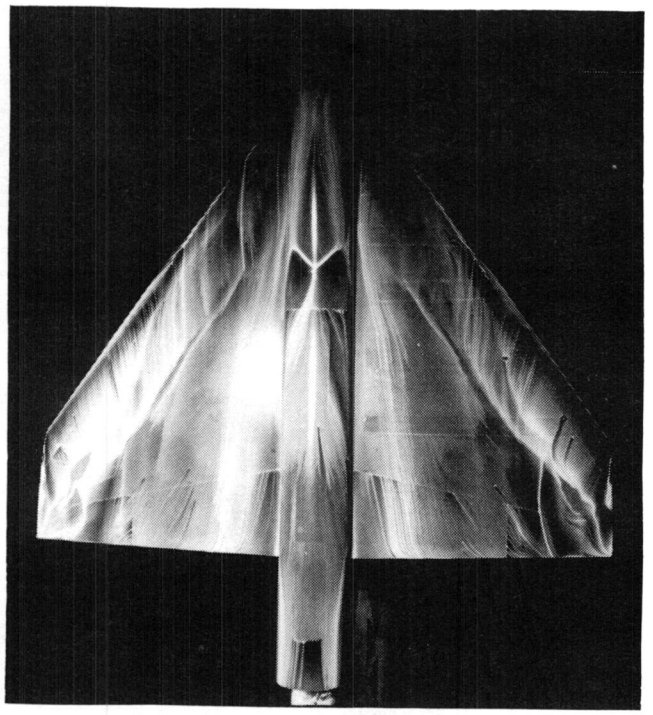

Figure 37. Oil flow visualization of wing/body; $M_\infty = 1.2$, $\alpha = 12.0°$.

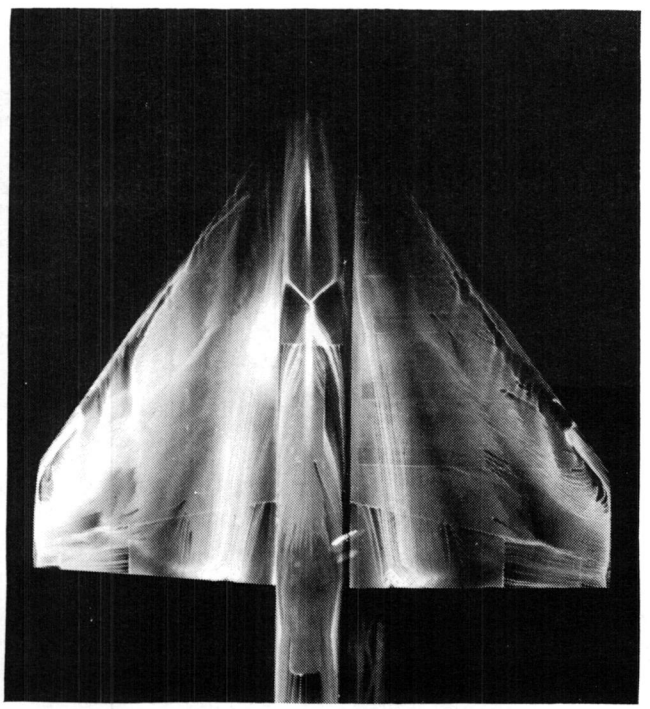

Figure 38. Oil flow visualization of wing/body; $M_\infty = 1.2$, $\alpha = 16.0°$.

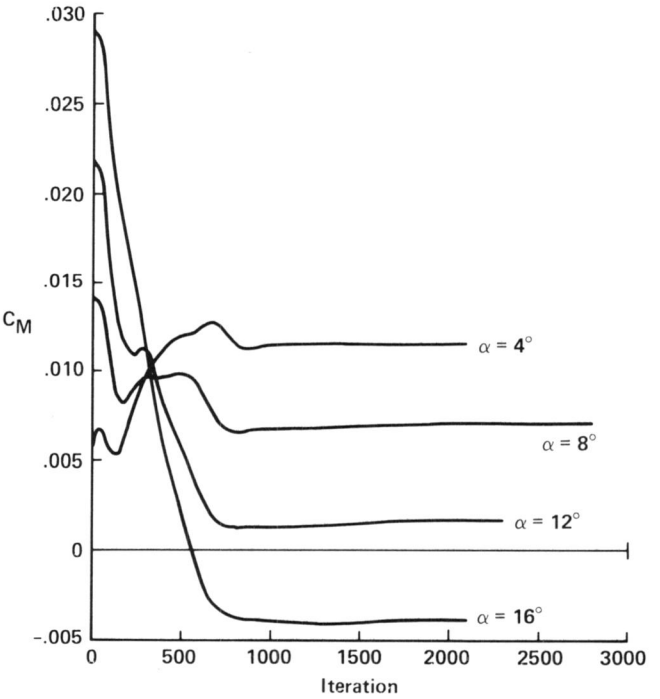

Figure 39. Pitching moment history for wing/body, $M_\infty = 1.2$.

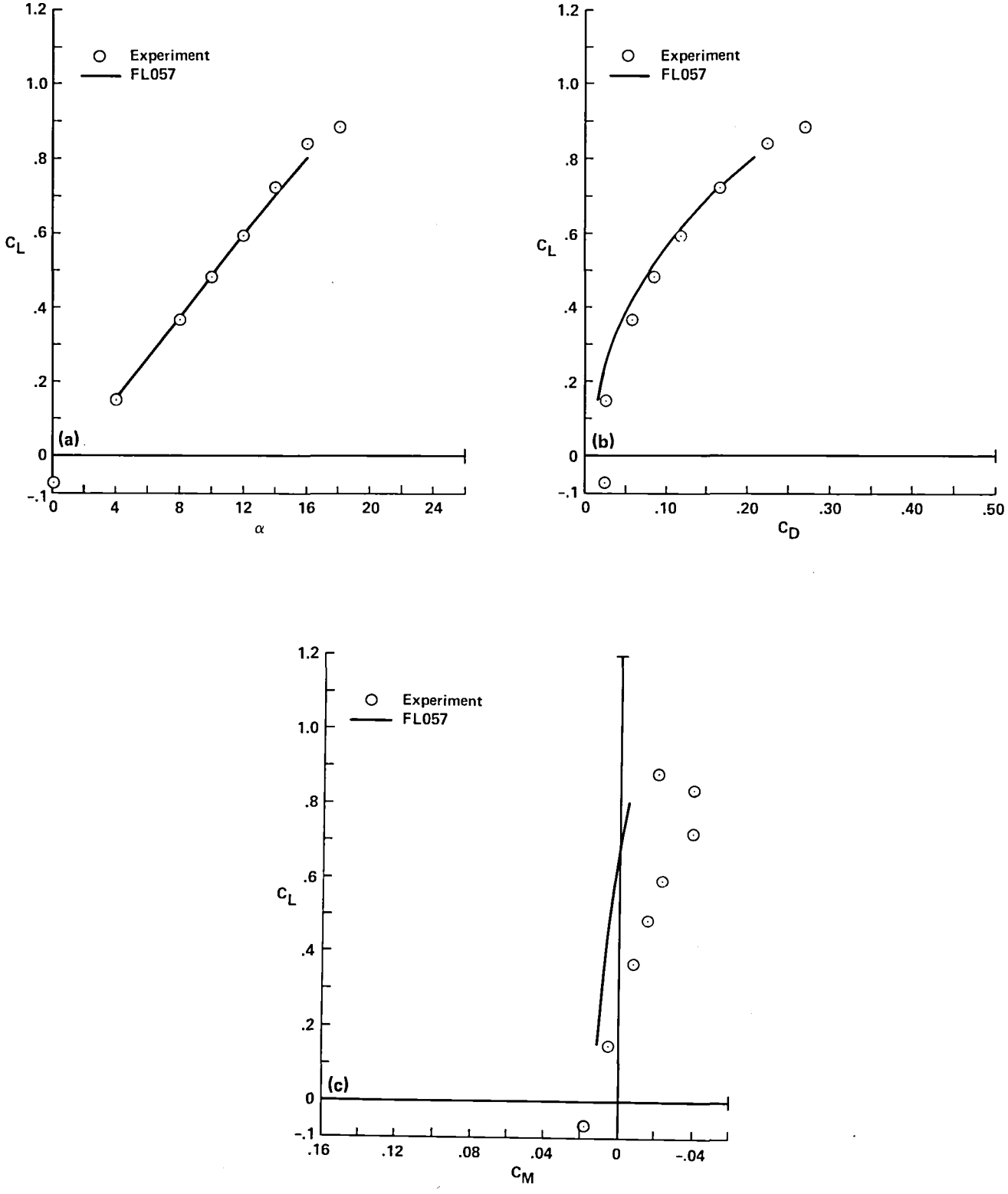

Figure 40. Experiment–CFD forces and moments for wing/body, $M_\infty = 1.2$; (a) lift curve, (b) drag polar, (c) moment curve.

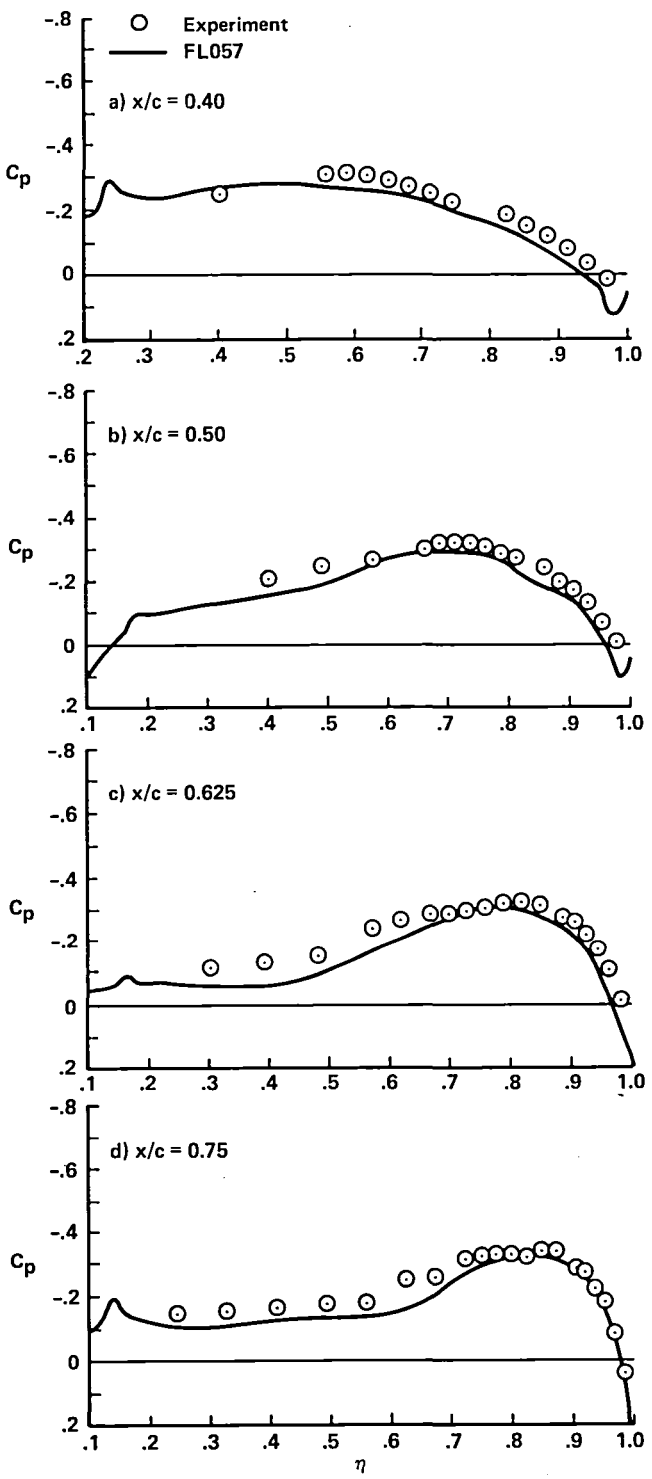

Figure 41. Upper surface pressure distributions for wing/body/chine; $M_\infty = 1.2$, $\alpha = 4.0°$.

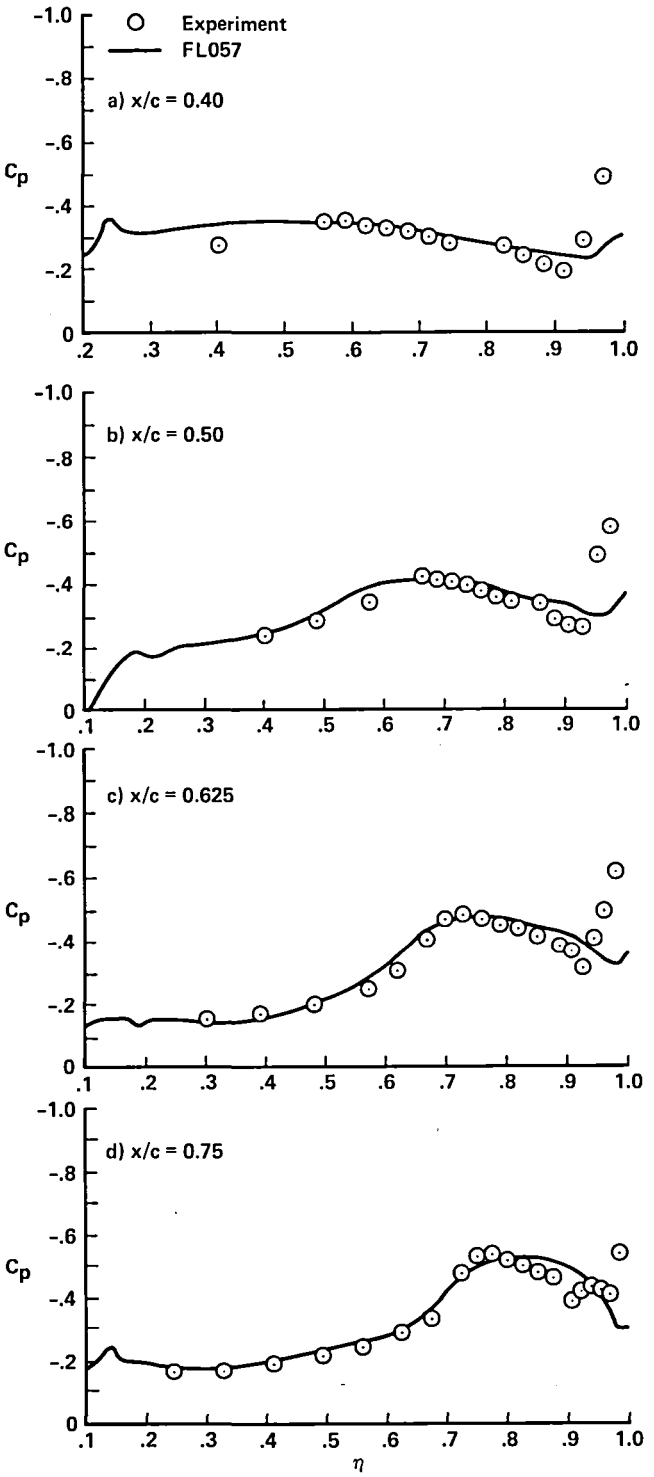

Figure 42. Upper surface pressure distributions for wing/body/chine; $M_\infty = 1.2$, $\alpha = 8.0°$.

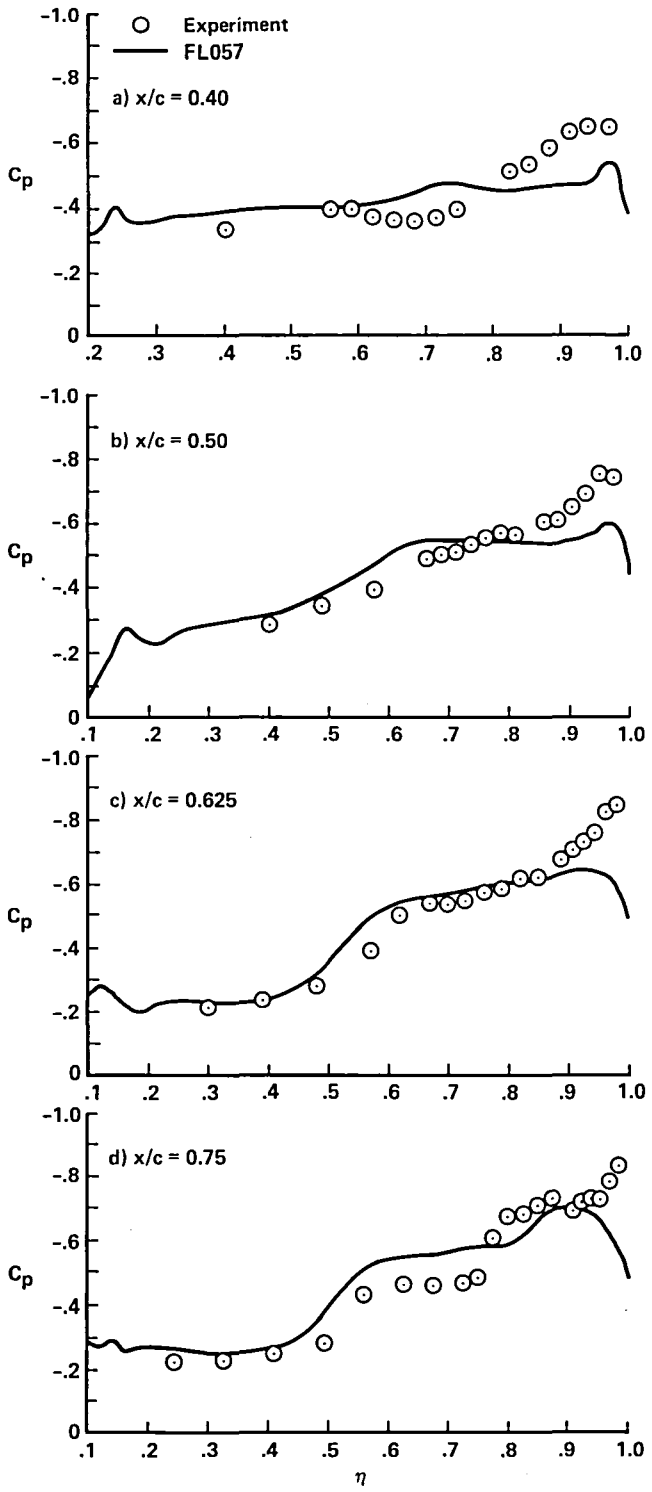

Figure 43. Upper surface pressure distributions for wing/body/chine; $M_\infty = 1.2$, $\alpha = 12.0°$.

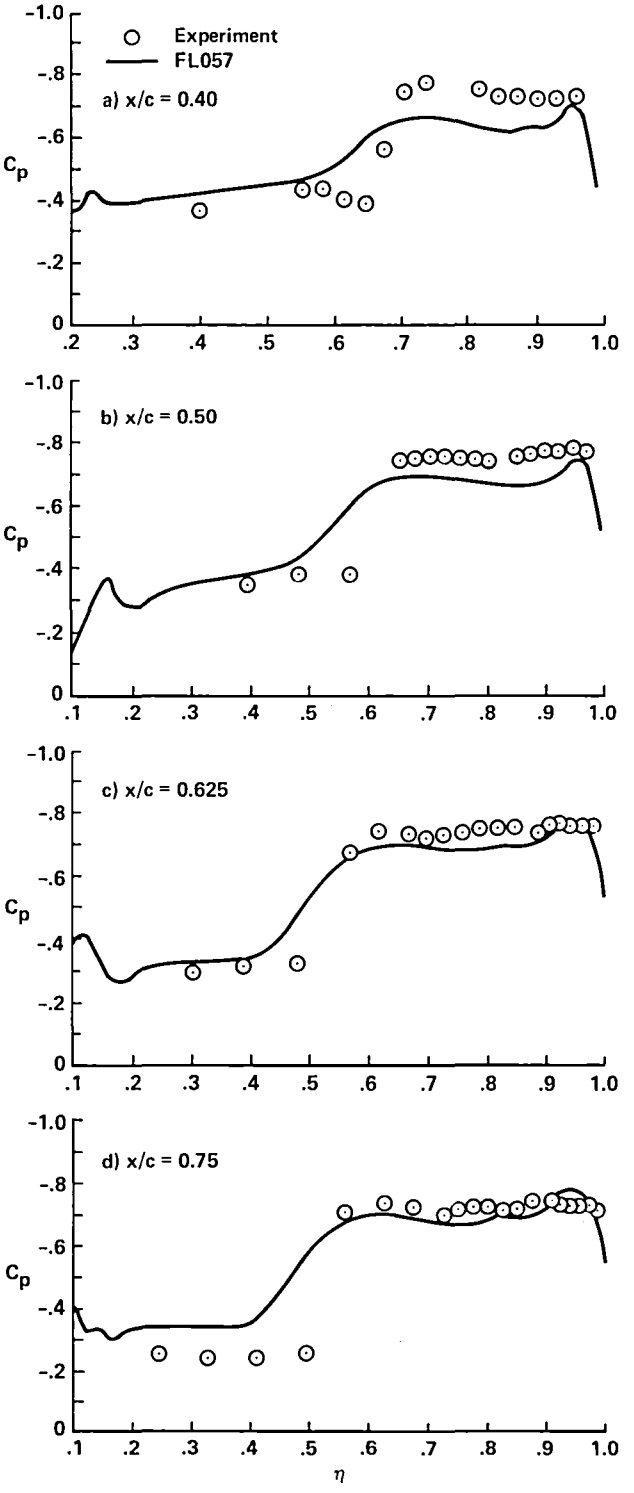

Figure 44. Upper surface pressure distributions for wing/body/chine; $M_\infty = 1.2$, $\alpha = 16.0°$.

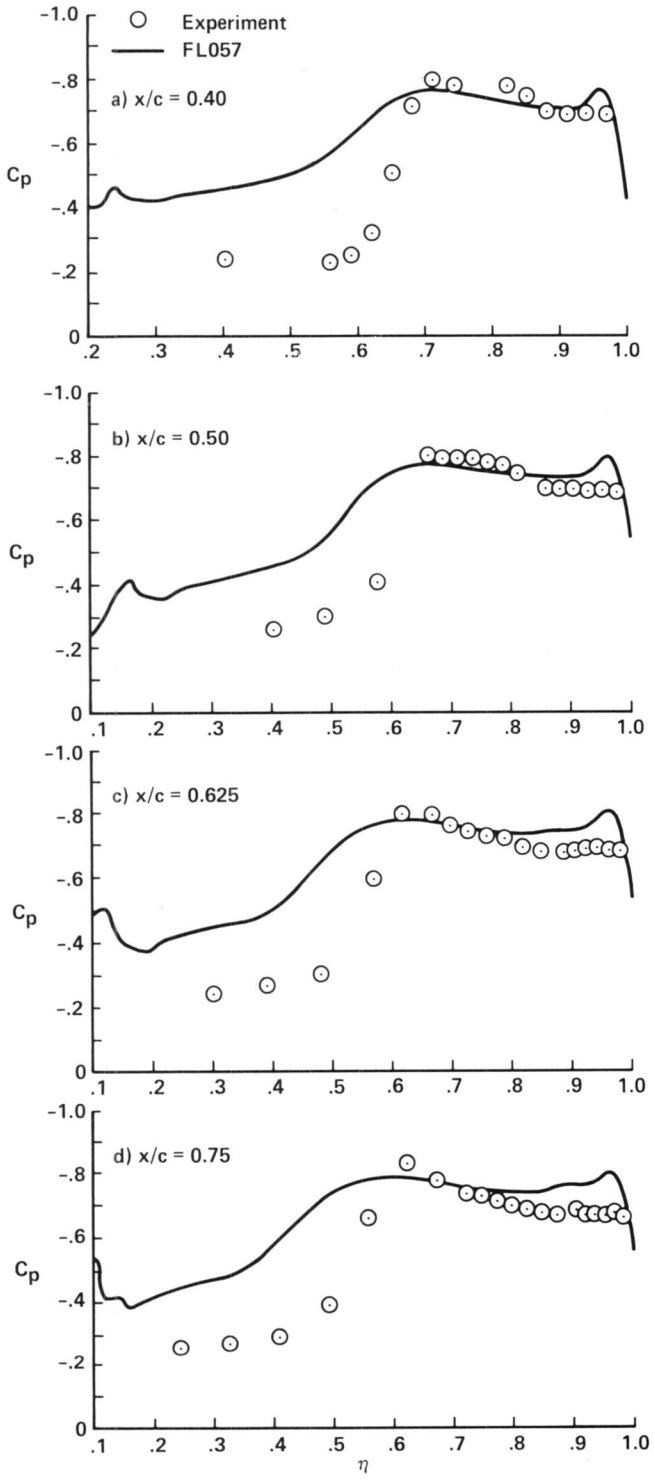

Figure 45. Upper surface pressure distributions for wing/body/chine; $M_\infty = 1.2$, $\alpha = 20.0°$.

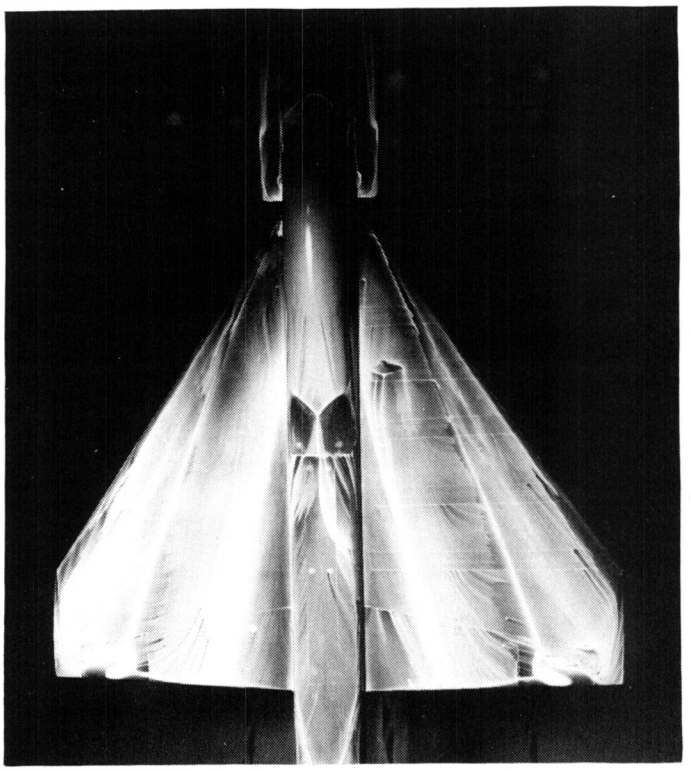

Figure 46. Oil flow photography for wing/body/chine; $M_\infty = 1.2$, $\alpha = 20.0°$.

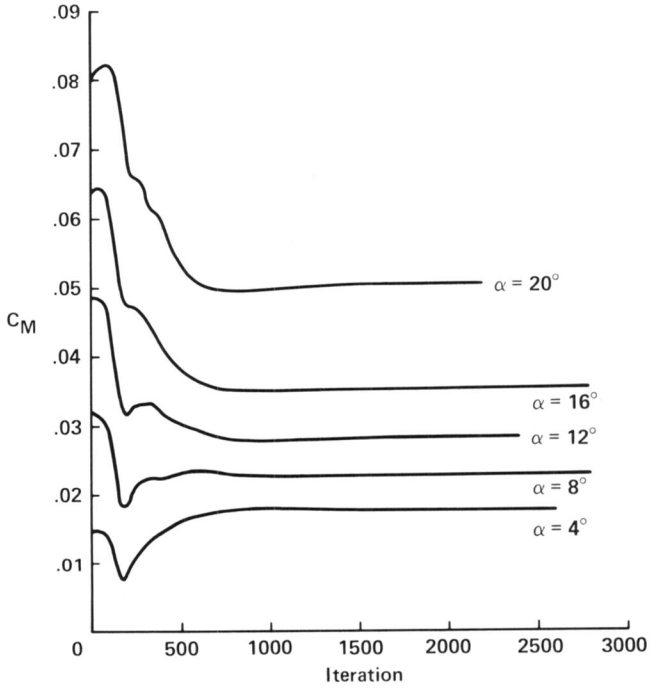

Figure 47. Pitching moment history for wing/body/chine, $M_\infty = 1.2$.

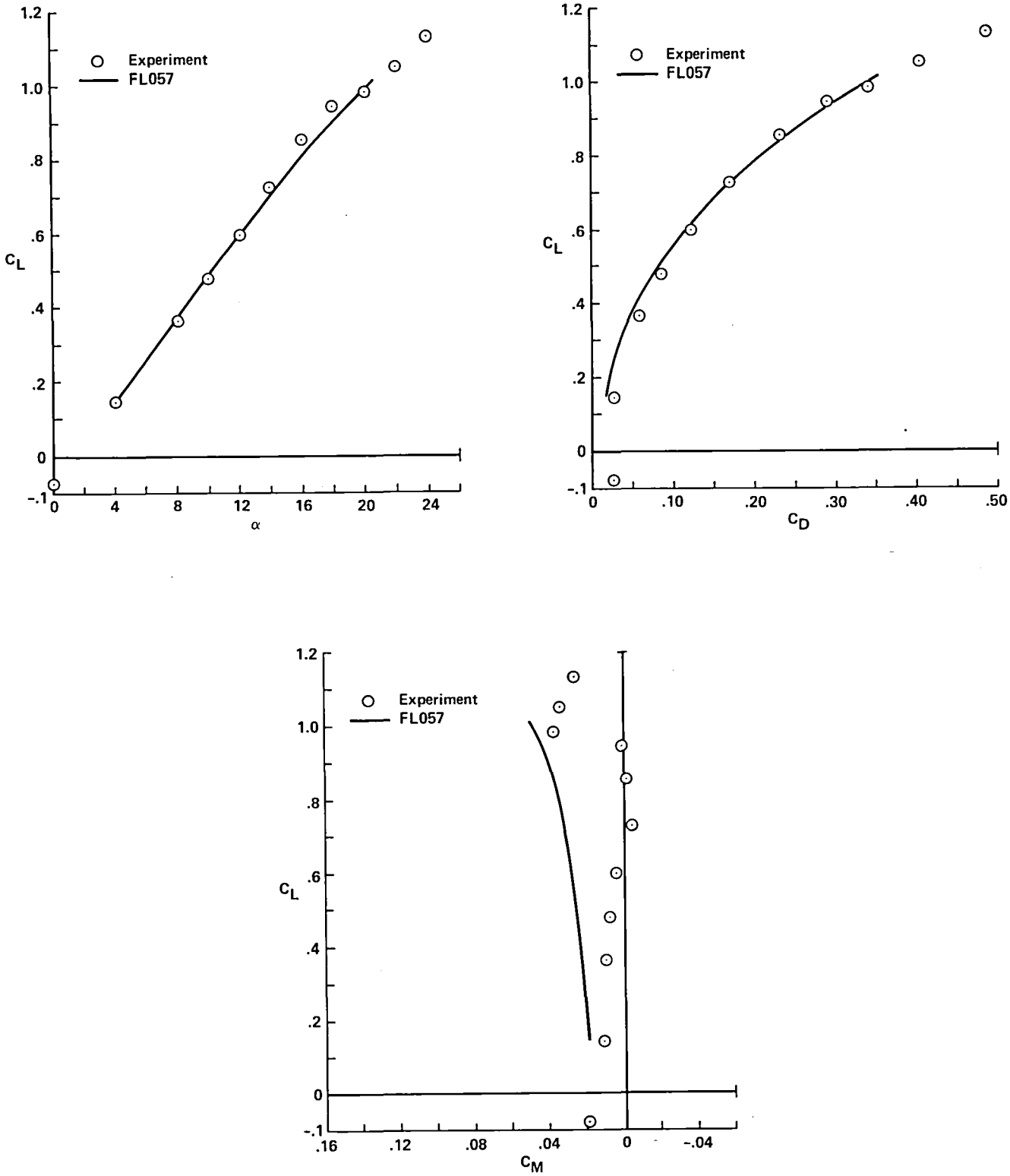

Figure 48. Experiment–CFD forces and moments for wing/body/chine, $M_\infty = 1.2$; (a) lift curve, (b) drag polar, (c) moment curve.

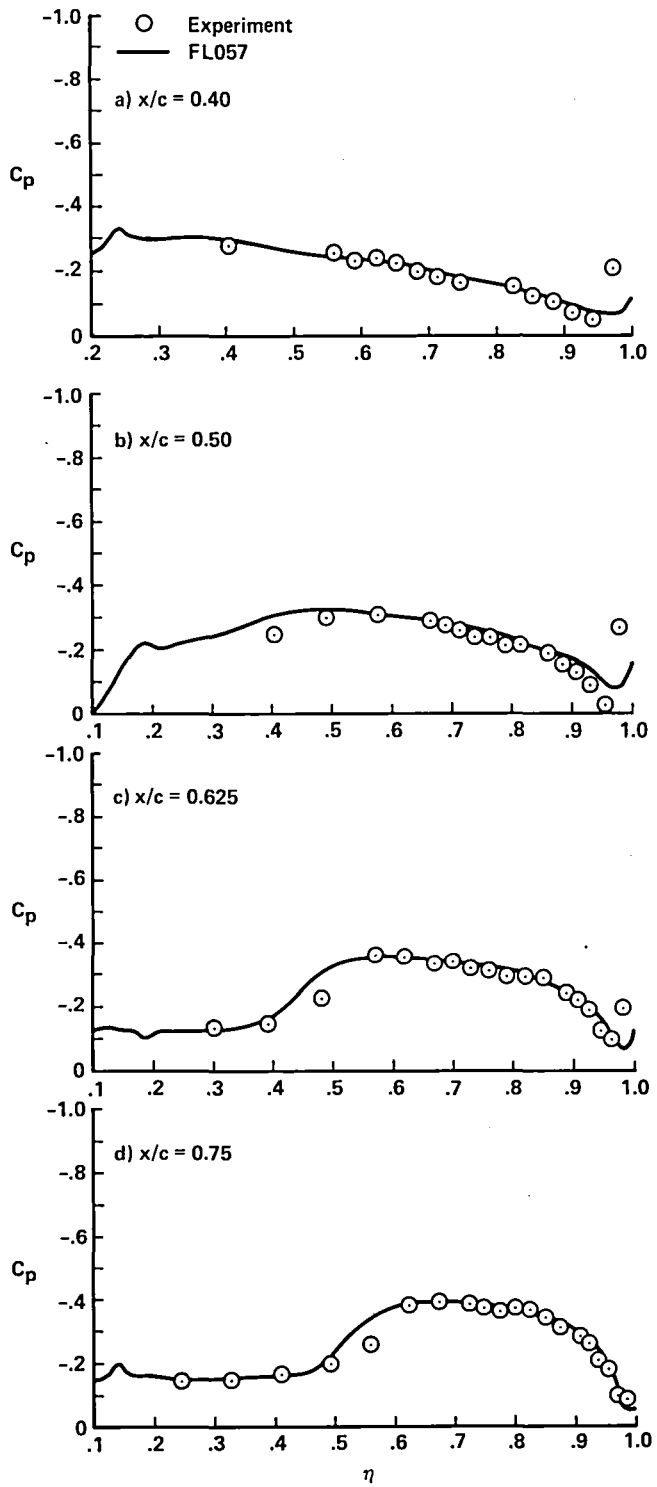

Figure 49. Upper surface pressure distributions for wing/body/chine; $M_\infty = 1.4$, $\alpha = 8.0°$.

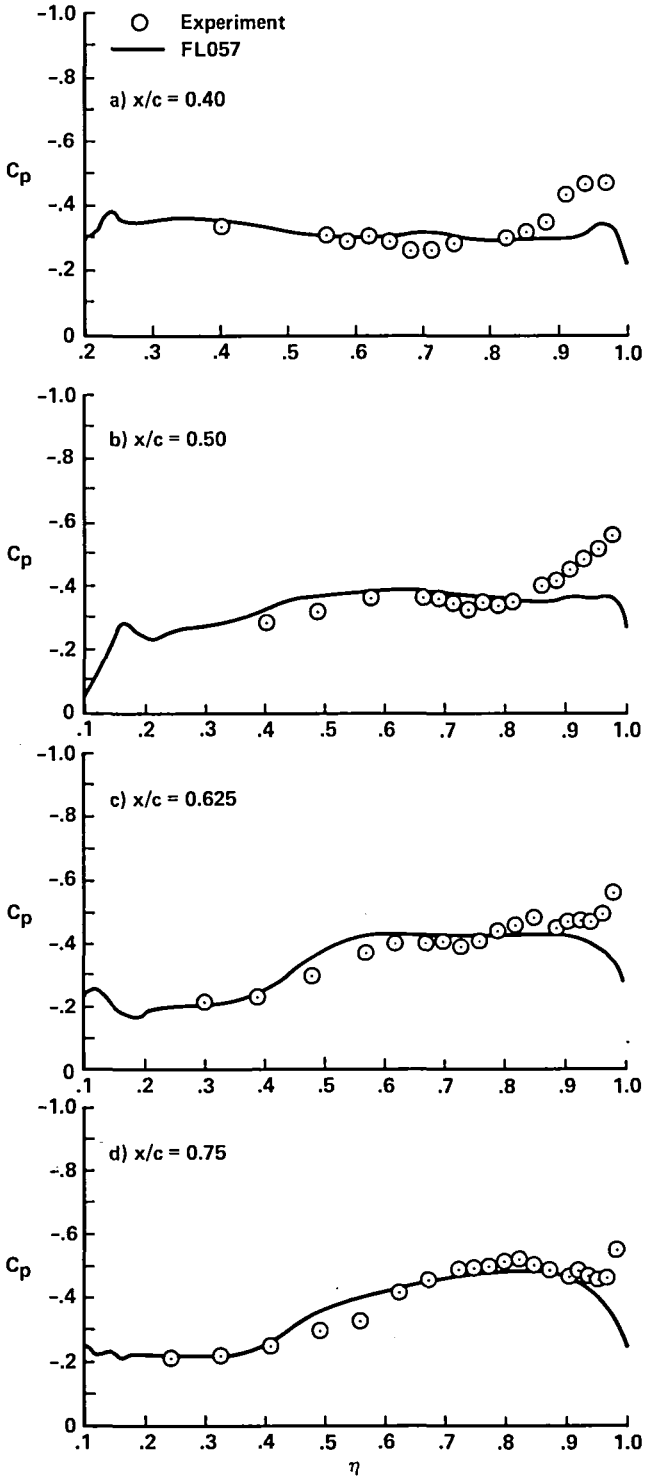

Figure 50. Upper surface pressure distributions for wing/body/chine; $M_\infty = 1.4$, $\alpha = 12.0°$.

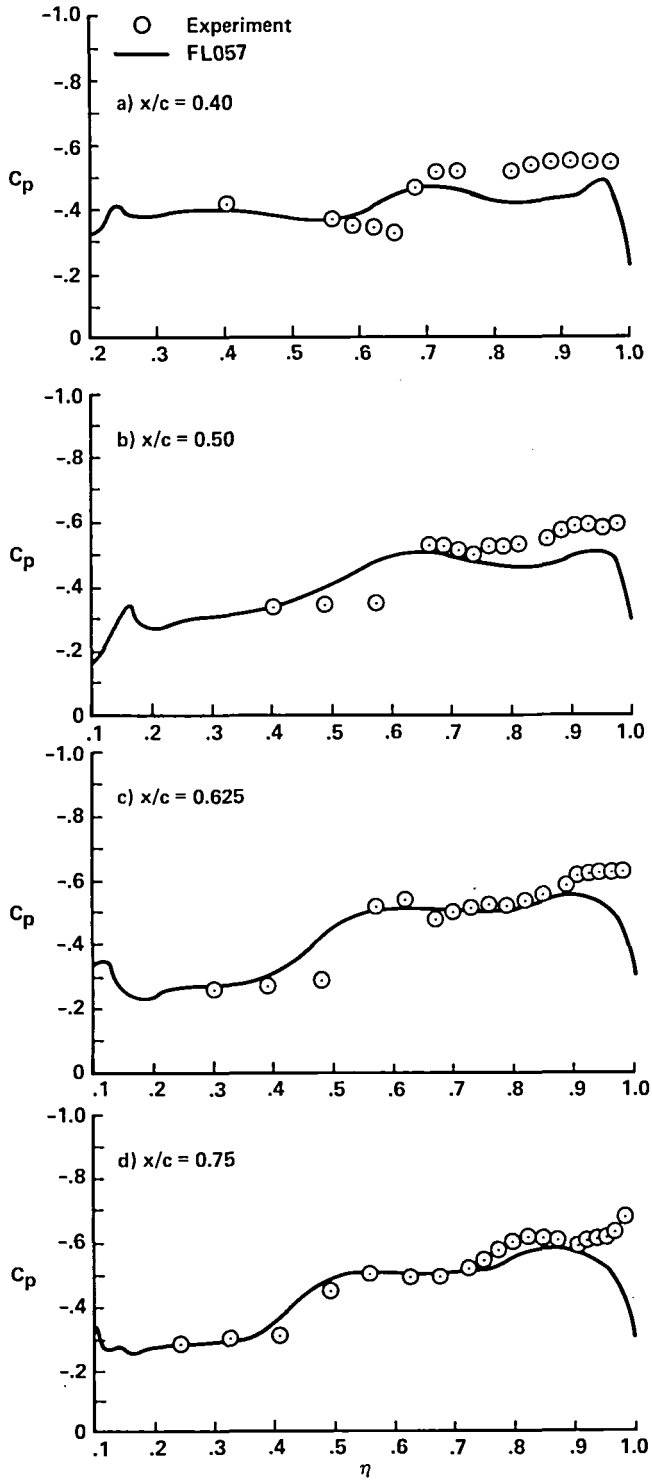

Figure 51. Upper surface pressure distributions for wing/body/chine; $M_\infty = 1.4$, $\alpha = 16.0°$.

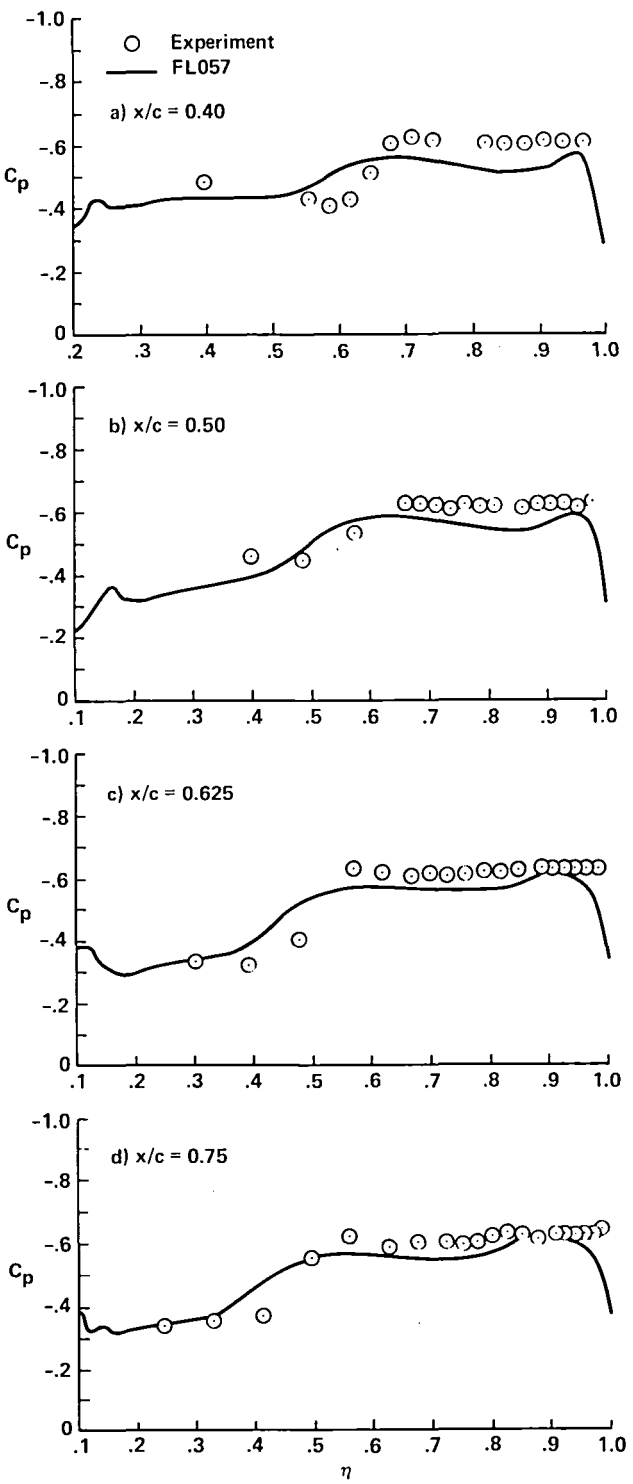

Figure 52. Upper surface pressure distributions for wing/body/chine; $M_\infty = 1.4$, $\alpha = 20.0°$.

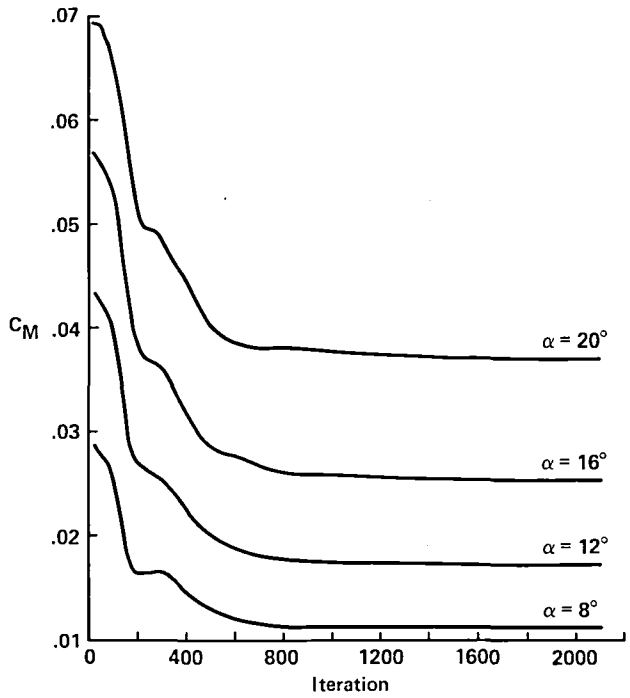

Figure 53. Pitching moment history for wing/body/chine, $M_\infty = 1.4$.

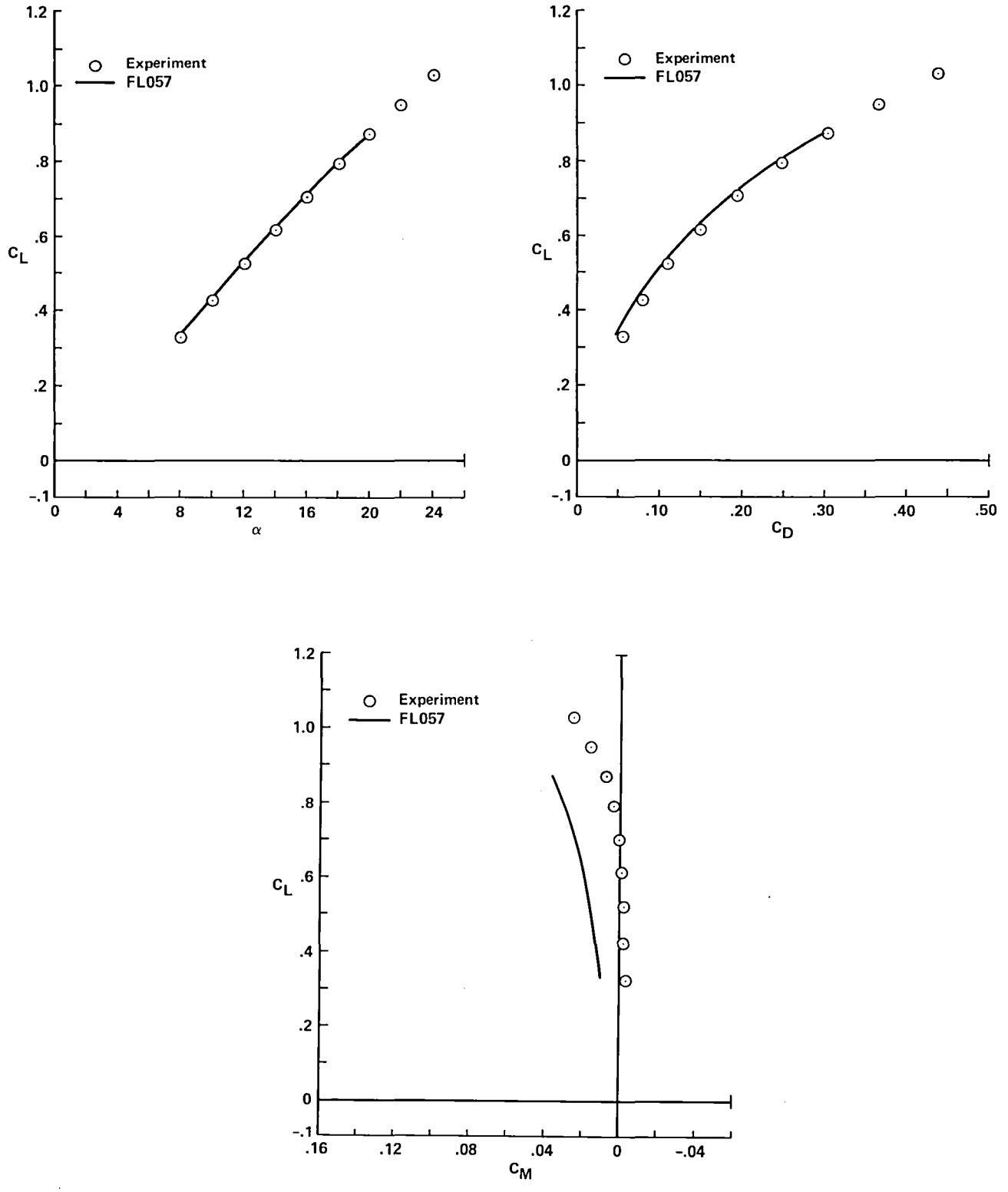

Figure 54. Experiment–CFD forces and moments for wing/body/chine, $M_\infty = 1.4$; (a) lift curve, (b) drag polar, (c) moment curve.

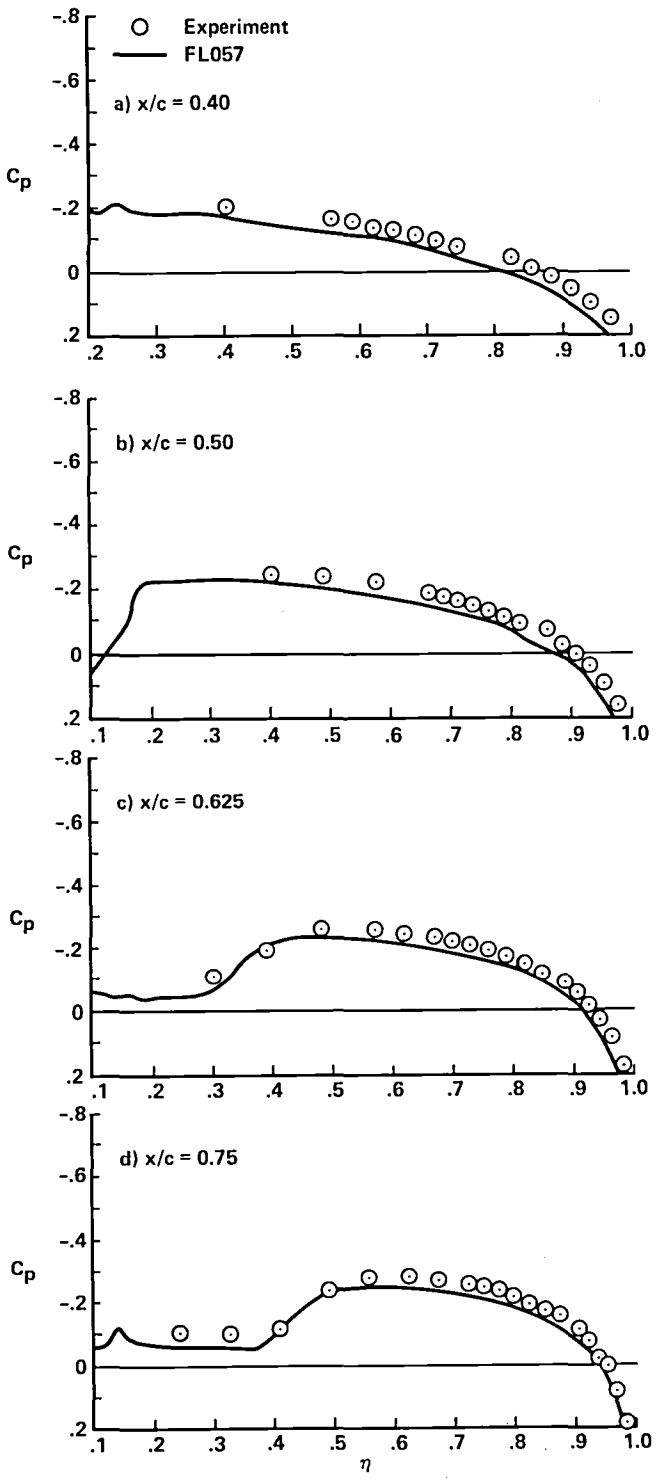

Figure 55. Upper surface pressure distributions for wing/body/chine; $M_\infty = 1.6$, $\alpha = 4.0°$.

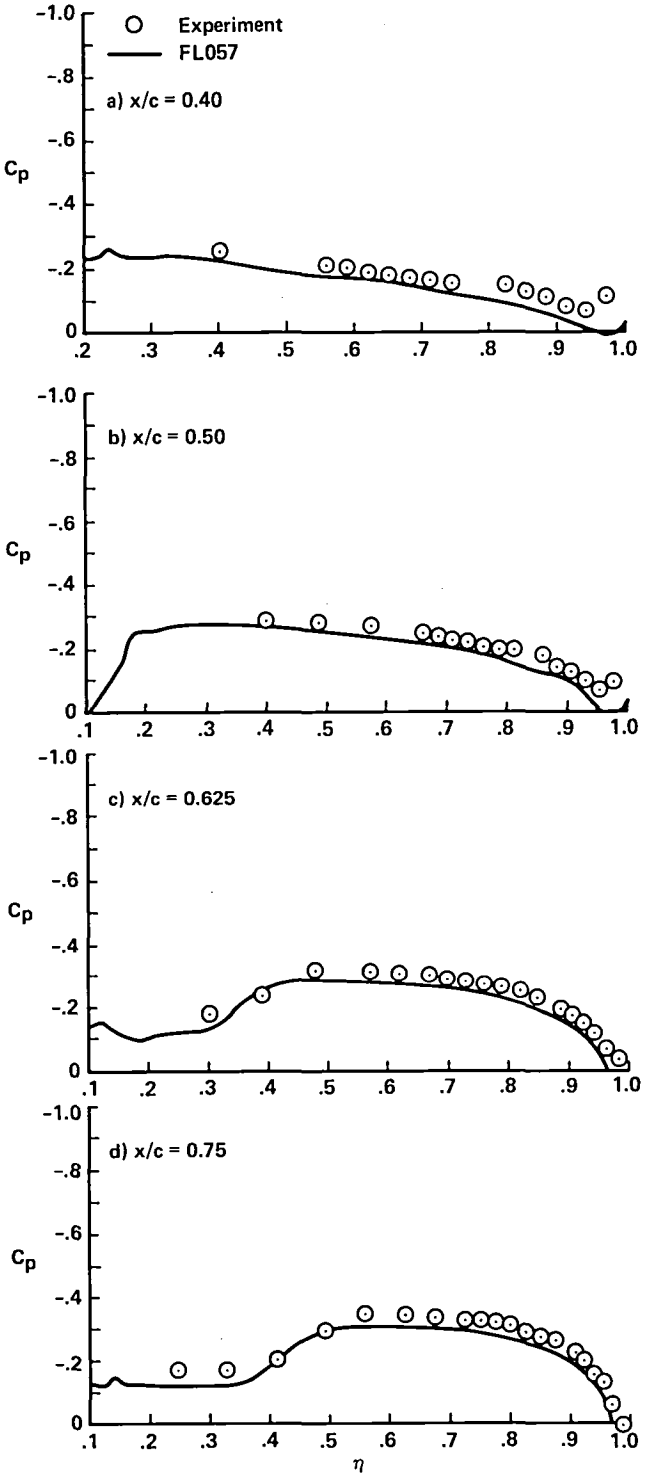

Figure 56. Upper surface pressure distributions for wing/body/chine; $M_\infty = 1.6$, $\alpha = 8.0°$.

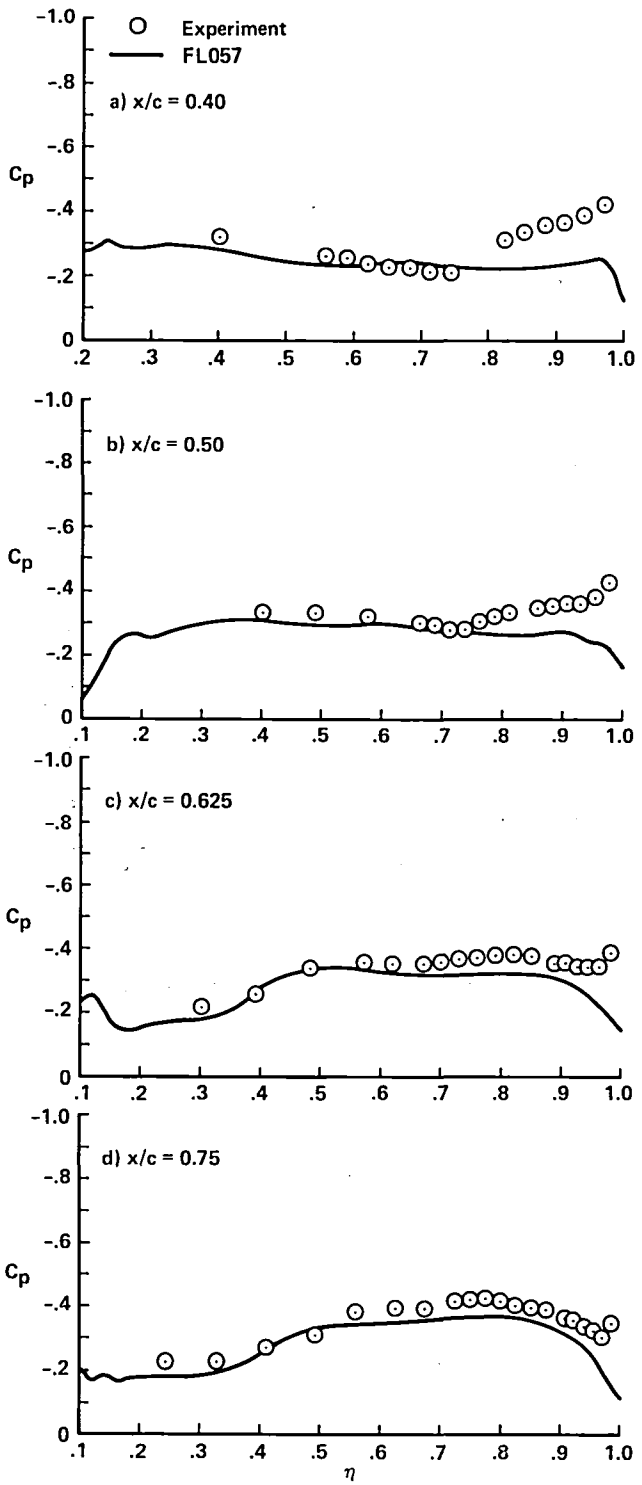

Figure 57. Upper surface pressure distributions for wing/body/chine; $M_\infty = 1.6$, $\alpha = 12.0°$.

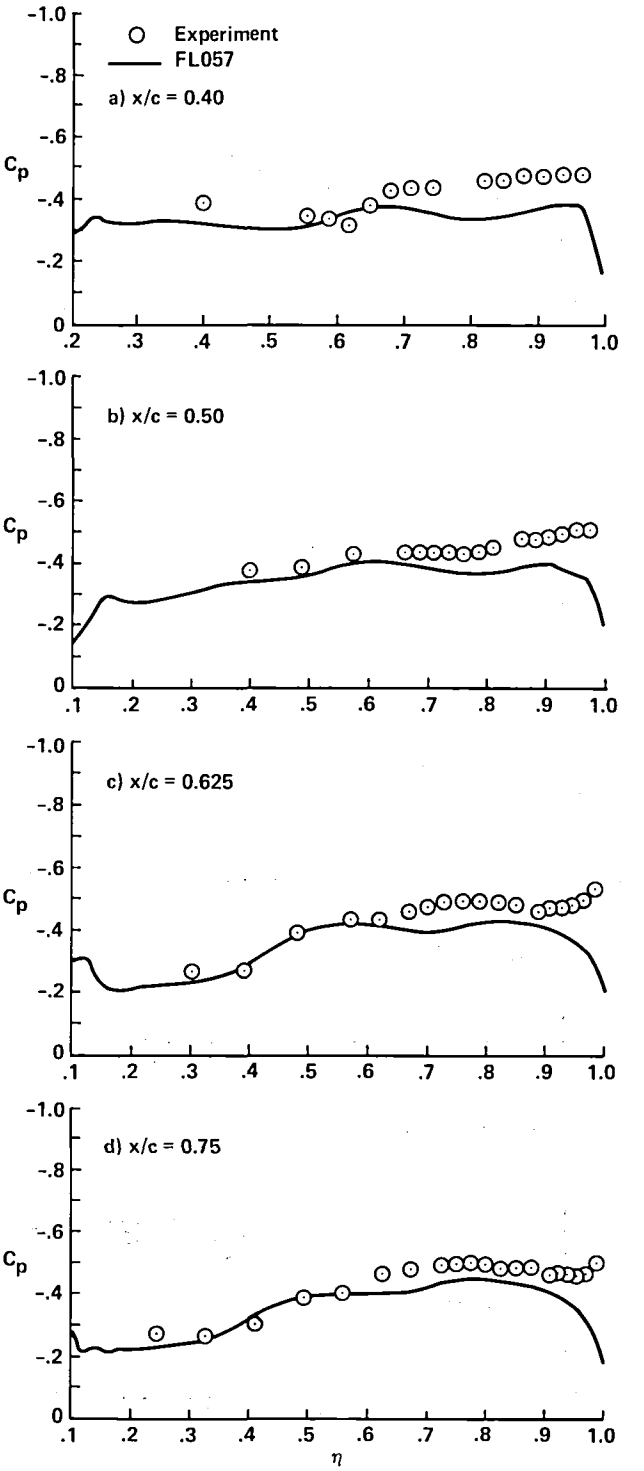

Figure 58. Upper surface pressure distributions for wing/body/chine; $M_\infty = 1.6$, $\alpha = 16.0°$.

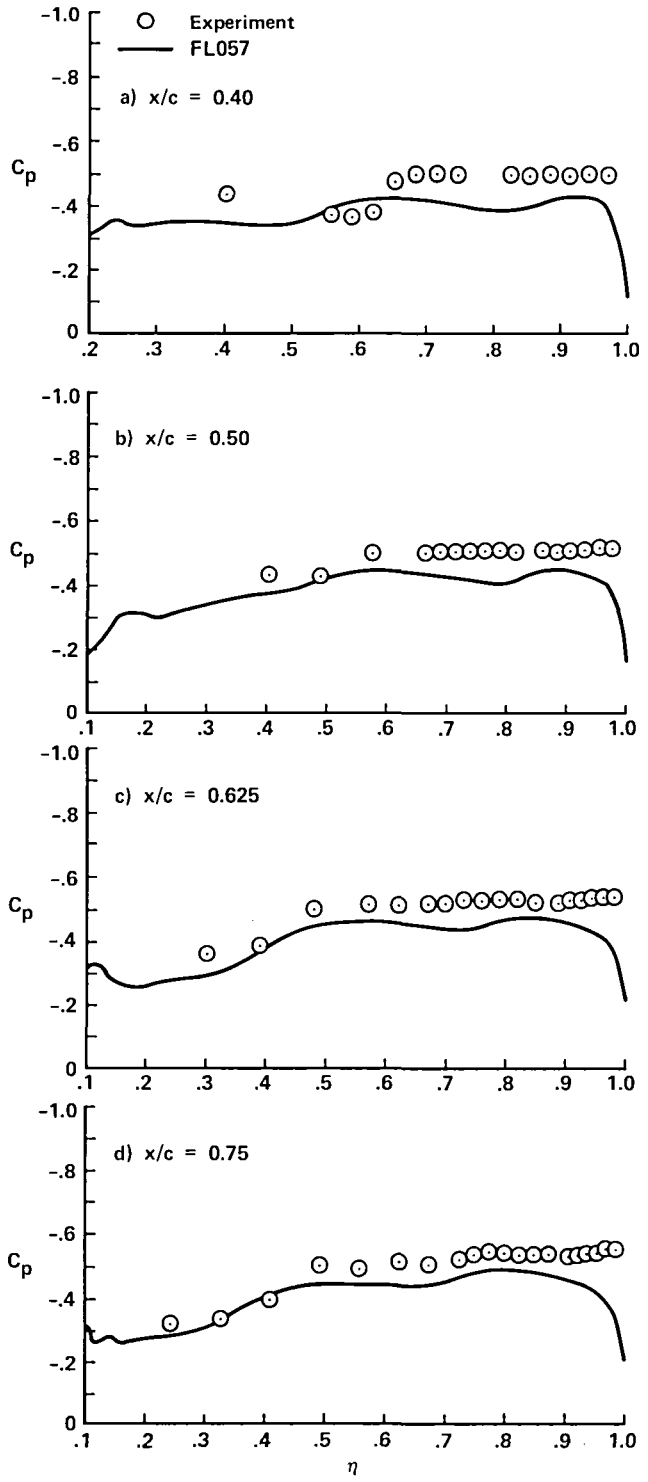

Figure 59. Upper surface pressure distributions for wing/body/chine; $M_\infty = 1.6$, $\alpha = 20.0°$.

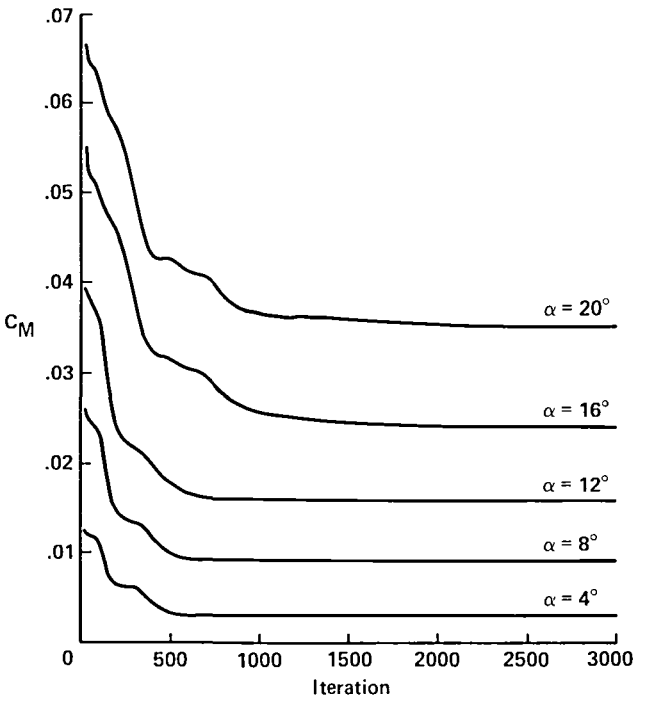

Figure 60. Pitching moment history for wing/body/chine, $M_\infty = 1.6$.

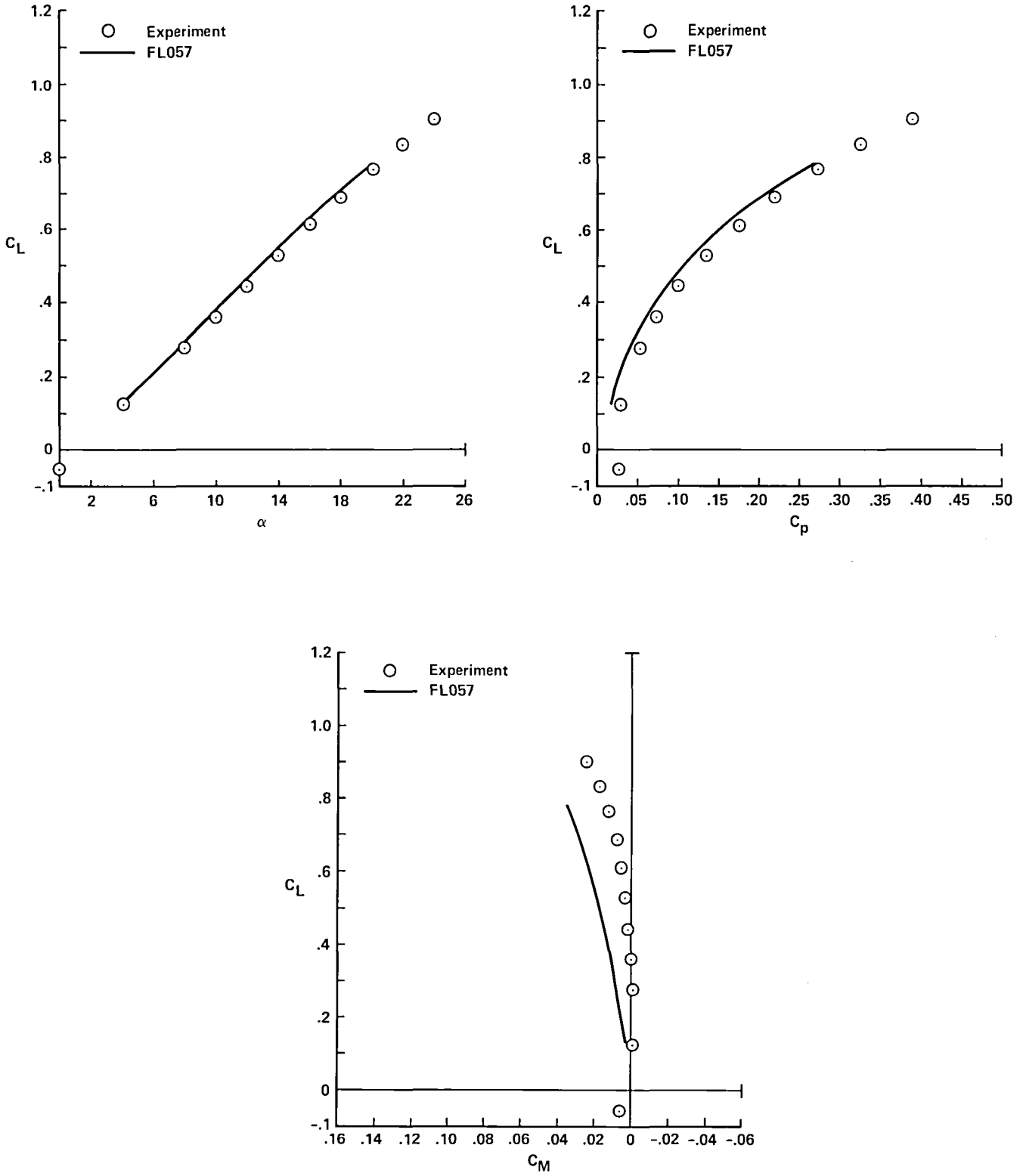

Figure 61. Experiment–CFD forces and moments for wing/body/chine, $M_\infty = 1.6$; (a) lift curve, (b) drag polar, (c) moment curve.

REPORT DOCUMENTATION PAGE

Form Approved
OMB No. 0704-0188

1. AGENCY USE ONLY *(Leave blank)*	2. REPORT DATE	3. REPORT TYPE AND DATES COVERED
	November 1991	Technical Publication

4. TITLE AND SUBTITLE

Transonic and Supersonic Euler Computations of Vortex-Dominated Flow Fields About a Generic Fighter

5. FUNDING NUMBERS

505-60-11

6. AUTHOR(S)

Aga M. Goodsell and John E. Melton

7. PERFORMING ORGANIZATION NAME(S) AND ADDRESS(ES)

Ames Research Center
Moffett Field, CA 94035-1000

8. PERFORMING ORGANIZATION REPORT NUMBER

A-90161

9. SPONSORING/MONITORING AGENCY NAME(S) AND ADDRESS(ES)

National Aeronautics and Space Administration
Washington, DC 20546-0001

10. SPONSORING/MONITORING AGENCY REPORT NUMBER

NASA TP-3156

11. SUPPLEMENTARY NOTES

Point of Contact: Aga M. Goodsell, Ames Research Center, MS 227-2, Moffett Field, CA 94035-1000
(415) 604-3621 or FTS 464-3621

12a. DISTRIBUTION/AVAILABILITY STATEMENT

Unclassified — Unlimited
Subject Category 02

12b. DISTRIBUTION CODE

13. ABSTRACT *(Maximum 200 words)*

Flow fields about a generic fighter model have been computed using FLO57, a three-dimensional, finite-volume Euler code. Computed pressure coefficients, forces, and moments at several Mach numbers—0.6, 0.8, 1.2, 1.4, and 1.6—are compared with wind tunnel data over a wide range of angles of attack in order to determine the applicability of the code for the analysis of fighter configurations.Two configurations were studied, a wing/body and a wing/body/chine. FLO57 predicted pressure distributions, forces, and moments well at low angles of attack, at which the flow was fully attached. The FLO57 predictions were also accurate for some test conditions once the leading-edge vortex became well established. At the subsonic speeds, FLO57 predicted vortex breakdown earlier than that seen in the experimental results. Placing the chine on the forebody delayed the onset of bursting and improved the correlation between numerical and experimental data at the subsonic conditions.

14. SUBJECT TERMS	15. NUMBER OF PAGES
Vortical flows, CFD validation, Euler computations	44
	16. PRICE CODE A03

17. SECURITY CLASSIFICATION OF REPORT	18. SECURITY CLASSIFICATION OF THIS PAGE	19. SECURITY CLASSIFICATION OF ABSTRACT	20. LIMITATION OF ABSTRACT
Unclassified	Unclassified		

NSN 7540-01-280-5500

Standard Form 298 (Rev. 2-89)
Prescribed by ANSI Std. Z39-18
298-102

NASA-Langley, 1991